

CLARKSON UNIVERSITY

Poisson-Nernst-Planck Model for Simulating Ionic
Current through the Nanopore in a Semiconductor
Membrane

A Thesis by

Alexey Nikolaev

Department of Physics

Submitted in partial fulfillment of the requirements

for the degree of

Master of Science

Physics

June 2011

Accepted by the Graduate School

Date

Dean

The undersigned have examined the thesis entitled “Poisson-Nernst-Planck Model for Simulating Ionic Current through the Nanopore in a Semiconductor Membrane” presented by Alexey Nikolaev, a candidate for the degree of Master of Science, and hereby certify that it is worthy of acceptance.

Date

Maria Gracheva (Advisor)

Daniel ben-Avraham

Vladimir Privman

Igor Sokolov

Abstract

Nanopores, biological and artificial, provide capabilities for detection and identification of biological analyte molecules, which are electrophoretically driven through the pore. Apart from the application as a biosensor, electrically tunable nanopores may be used for controlling the motion of a single biomolecule, which is translocating through the pore, and also for varying the ionic current flowing through it.

In this work, we develop a model for simulating ionic current through nanopore in a semiconductor membrane. The approach is based on the Poisson-Nernst-Planck (PNP) theory, which describes ionic transport in the electrolyte. The model provides a general method for ionic current simulation for semiconductor-based nanodevices with arbitrary geometry, however we are primarily focused on nanoporous devices.

In the first part, we consider a nanopore in a solid-state membrane, which is made of two layers of n- and p- heavily doped silicon material. We apply the electrostatic model to calculate ionic concentrations and electric potential distribution in the whole system. The ionic current through the pore is estimated using a 1-dimensional model. The system is investigated at different voltages applied to the silicon layers, and for three possible geometries of the pore. We provide a systematic comparison of these voltage/geometry configurations, and make conclusions about our ability to control properties of the device, such as the current rectification ratio, and potential variation in the channel.

In the second part, we provide a detailed description of the numerical techniques, which are needed to simulate ionic current using the Poisson-Nernst-Planck method:

a finite-difference discretization of the Nernst-Planck equations, boundary conditions, and a self-consistent iterative procedure. After that, we compare the PNP model with the results of the 1D technique, which were obtained previously. Finally, we consider a different membrane structure, which has only one n-Si layer, “sandwiched” between two oxide layers.

In this system, the spacial distribution of ions in the channel and surface charge on the walls of the pore bear a resemblance to the distribution of electrons, holes and doping atoms in MOSFETs. We analyze the I-V characteristics, conductance, and trans conductance of this ionic transistor. The similarity between this device and solid-state transistors is discussed.

Acknowledgments

I would like to acknowledge and extend my heartfelt gratitude to persons who have made the completion of this work possible.

Firstly, I would like to thank my adviser Professor Maria Gracheva for guidance and support. This work was my first big scientific project, I learned a lot about professional research work and scientific methods from Professor Gracheva, and truly grateful for this experience.

Professor Igor Sokolov, Professor Daniel ben-Avraham, and Professor Vladimir Privman, for taking the time to serve on the thesis defense committee.

Professors of Physics and Mathematics Departments at Clarkson University for helpful and insightful discussions.

Contents

Objective	1
1 Introduction	2
1.1 Applications of Nanopores	2
1.1.1 Biological ion channels	3
1.1.2 α -hemolysin	3
1.1.3 Artificial Nanopores	5
1.2 Models and Simulation methods	6
1.2.1 Poisson-Boltzmann (PB) theory	7
1.2.2 Poisson-Nernst-Planck (PNP) theory	9
1.2.3 Computer simulations	10
2 Model of semiconductor heterostructures	12

3	Physical model	19
3.1	Membrane composition	19
3.2	Mathematical formulation of the problem	21
3.2.1	Poisson's equation	21
3.2.2	Concentrations of electrons and holes in silicon	21
3.2.3	Concentrations of ions	22
3.2.4	Boundary Conditions	24
4	Electrostatic problem	26
4.1	Introduction	26
4.1.1	Model	27
4.1.2	Computational method	27
4.1.3	Nanopore geometries and membrane biases	28
4.2	Results and discussion	29
4.2.1	Electrostatic potential and ionic concentration	29
4.2.2	Characterization of the electrostatic potential in the nanopore	31
4.2.3	Ionic current-voltage characteristics and rectification ratios . .	35

5	Poisson-Nernst-Planck approach	39
5.1	Discretization of the Nernst-Planck equations.	40
5.1.1	Ionic current density.	40
5.1.2	Finite-Difference Discretization.	41
5.1.3	Nernst-Planck equation in 1D.	41
5.1.4	Nernst-Planck equation in 3D.	42
5.1.5	Nernst-Planck equation in 3D and Gauss's divergence theorem	43
5.1.6	Boundary Conditions	44
5.1.7	Current through the pore in YZ cross-section.	44
5.2	Iterative method	45
5.2.1	Data representation	45
5.2.2	Convergence condition	45
5.2.3	Iterative procedure	46
5.3	One-dimensional method for ionic current calculation, and evalua- tion of its validity.	48
5.3.1	I-V characteristics of the 1D and 3D methods	49
5.3.2	Quantitative estimation of the difference between 1D and 3D methods	50

5.4	Oxide Membrane.	52
5.5	Oxide – n-Si – oxide Membrane.	53
5.5.1	I-V curves and transconductance.	55
5.5.2	Conductance for small drain-source bias V_{DS}	56
	Conclusions	59
	Bibliography	61
A	Comparison of I-V curves obtained from 1D and 3D methods, and the quantitative estimation of their difference.	66

List of Tables

4.1	Parameters and constants	38
5.1	Normalized RMS deviations of 1D methods from the 3D PNP method	51

Objective

The goal of this work is to develop a model for calculation of the ionic current through the nanopore in a semiconductor membrane. The basis of our model is the Poisson-Nernst-Planck theory, which is successfully used for ionic current simulation [39–48]. We want to apply this theory to model ionic current in nanopores in multilayered semiconductor membranes. Our main objective is to estimate properties of the modeled nanopores, and search for better designs and devices, which may be efficiently control by voltages applied to the membrane.

Chapter 1

Introduction

Since 90's, when experiments with α -hemolysin showed a possibility of nanopore-based DNA-sequencing [1], a substantial research work has been done in the area of physics of biological and artificial nanopores (see reviews [2], [3] and [4]). Although, this particular field of studies that is focused on biomolecule sensing is relatively modern, its theory is strongly rooted in well-developed disciplines of micro- and nanofluidics, semiconductor physics, biology and chemistry. We base our work on these theories, in attempt to make a successful model that will lead to new efficient nanopore designs, better understanding of artificial and biologic channels, and insights into biosensors.

1.1 Applications of Nanopores

Nanopores are an excellent example of nano-devices, which are able to interact efficiently with ions and biological molecules in aqueous solution. While permeating

through the pore, these molecules interact with the walls of the pore. Since ions and most of biological molecules in aqueous solution are charged, electrical interaction between these molecules and the nanopore surface is the crucial factor of the system.

1.1.1 Biological ion channels

While this work is focused on the properties of a nanopore in a semiconductor membrane, the most vivid example of the effectiveness of nanopores can be found in living cells, where concentrations of ions in the cytosol and the extracellular environment are regulated by numerous ion channels – biological nanopores.

Being able to respond to electrical and chemical signals, ion channels play a crucial role in cell functioning. Some of them have very high selectivity for a specific type of ions. And nature of this selectivity (for example, as in potassium channel) is a beautiful result of evolution, that must be inspirational for human-designed nano-bio-devices.

1.1.2 α -hemolysin

In 1996, Deamer, Branton, Kasianowicz, and colleagues demonstrated [1] that biological pore, formed by *Staphylococcus aureus* alpha-toxin (α -hemolysin), can be used for single-stranded DNA and RNA detection, and also the length of a strand may be determined from a measured ionic current blockade. It was possible, because of the geometric and electric properties of the channel. The smallest diam-

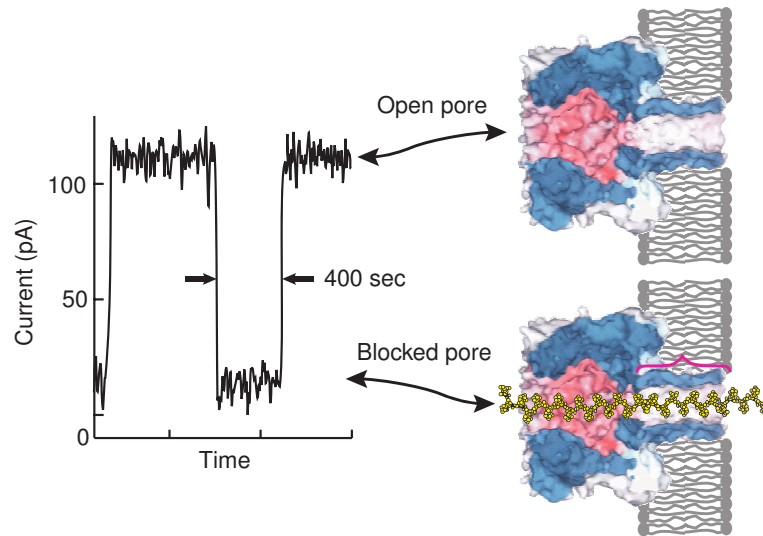


Figure 1.1: Ionic current blockade method using α -hemolysin (from [2]).

eter of the α -hemolysin pore is equal to 1.4 nm, which is less than the diameter of double-stranded DNA (2 nm). However, a single-stranded DNA molecule *can* translocate through the pore, and nucleotides of a strand move through it in sequential order, which was considered to be a promising technique for inexpensive DNA sequencing.

Later, the same ionic current blockade method was used successfully for polyA and polyC RNA discrimination [6] and similar results were obtained for several DNA polynucleotides [7]. However, it turned out that such discrimination was a consequence of the difference in the secondary structure of the polynucleotides [6]. Nevertheless, more sophisticated techniques should be developed for accurate biomolecule detection and analysis [2, 3].

1.1.3 Artificial Nanopores

Advances in the technology of semiconductor devices manufacturing provide a possibility to design artificial nanopores, which can be used to improve and enhance the existing ionic current blockade technique. Moreover, such devices may employ approaches borrowed from the traditional electronics, or more novel methods based on the interaction between a biomolecule and a solid-state device. Properties of the interface between a solid-state material and electrolyte are of the highest importance, the surface charge controlled by pH is the basic characteristic of the pore. Also, additional coating on the solid-state membrane [8] is a very powerful method to achieve needed properties of the surface.

Being more robust and variable than their biological counterparts, artificial nanopores are anticipated to be effective in single molecule detection, protein filtering and analysis of biomolecule properties [4, 9–12]. Semiconductor-based nanopores provide mechanisms to control ionic currents: Ionic diodes [13, 14], voltage-tunable ionic field-effect transistors [15–20] and pores in multilayered membranes [21, 22] have been proposed. Transverse electronic transport method [10, 23–25] was proposed for fast DNA sequencing. Another interesting group of nano-scale biosensors includes carbon nanotubes [26] and nanowires [27], which are based on the older idea of BioFET [28, 29] and ISFET [30–32]. All these approaches can find application in lab-on-a-chip devices.

Artificial nanodevices seem to be even more promising, since further improvements in manufacturing techniques are expected.

1.2 Models and Simulation methods

Our intention is to build a consistent 3D model of ionic current in a semiconductor nanopore, however, first, existing models must be examined. In this review, we start with models of electrical double layer (EDL), which is a very important concept in nanofluidics and interface science.

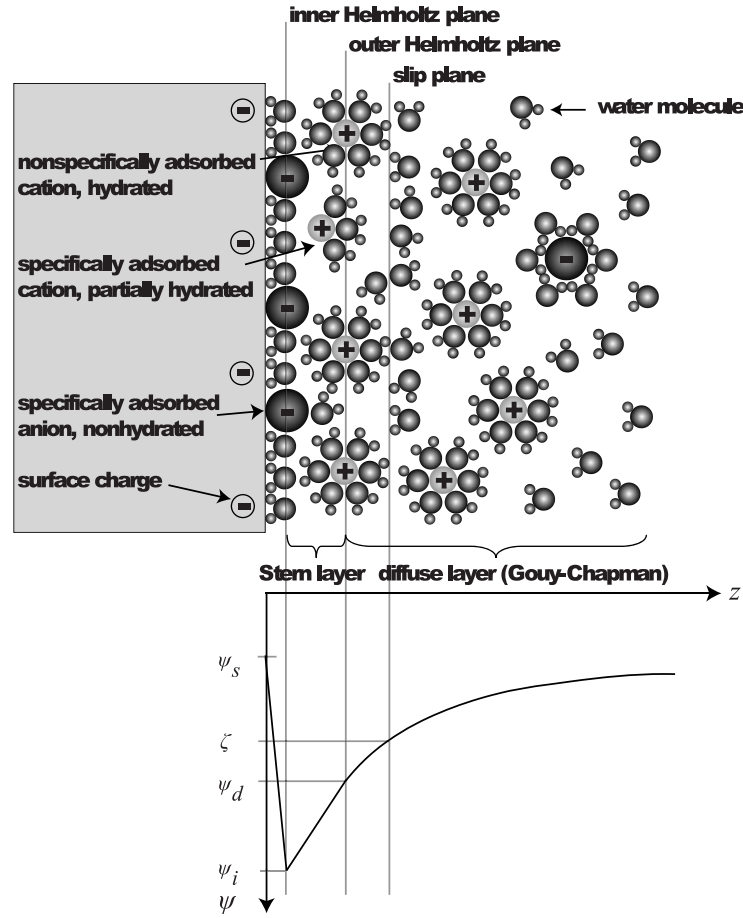


Figure 1.2: Gouy-Chapman-Stern model of the solid-electrolyte interface, and the potential distribution vs the distance from the wall [33].

A solid surface usually acquires some charge when immersed in electrolyte. This charge comes from chemical dissociation of surface groups or preferential physicochemical adsorption of electrolyte ions [33, 34]. Site-binding model [34, 35] is used to describe this process. Non-zero fixed charge located at the solid-liquid

interface, accumulates movable ions in the electrolyte, thus the electrical double layer (EDL) is formed. This representation of the electrolyte-solid interface is called Gouy-Chapman(-Stern) model (see [33, 34, 36] for more details).

1.2.1 Poisson-Boltzmann (PB) theory

Historically, Poisson-Boltzmann approach was used for modeling electrolyte at the boundary with a solid-state material. It describes a system in equilibrium, where chemical potential is constant in the electrolyte and, therefore, Boltzmann statistics for concentrations is applicable.

Poisson's equation

$$\nabla(\varepsilon \nabla \varphi) = -\frac{\rho}{\varepsilon_0}, \text{ where charge density } \rho = q \sum_{i=1}^N Z_i c_i,$$

together with expressions for the local concentrations of mobile ions in the diffuse layer

$$c_i = c_i^{bulk} \exp\left(-\frac{q Z_i (\varphi - \varphi^{bulk})}{kT}\right)$$

lead to the following equation:

$$\nabla(\varepsilon \nabla \varphi) = -\frac{q}{\varepsilon_0} \sum_{i=1}^N Z_i c_i^{bulk} \exp\left[-\frac{q Z_i (\varphi - \varphi^{bulk})}{kT}\right] \quad (1.1)$$

Here, c_i and Z_i are concentrations and the valence of the ionic species i . N is the total number of ionic species in the electrolyte. ε is the relative electric permittivity, and ε_0 is the absolute electric permittivity of the vacuum. q is the elementary charge, k is the Boltzmann constant.

The equation (1.1) is then solved for φ . It is usually assumed that $\varphi^{bulk} = 0$ [33, 34,

36]. Concentration c_i^{bulk} are obtained from the bulk electrolyte concentration (for example, for $[KCl]_0 = 0.1 \text{ M}$ electrolyte, $[Cl^-]^{bulk} = [K^+]^{bulk} = 0.1 \text{ M}$).

If one needs to find ionic concentrations in a cylindrical channel, it is possible to consider a cylindrical coordinate system. Then, for symmetric electrolyte (i.e. $Z \equiv Z_+ = -Z_-$) in a cylindrical channel, the equation (1.1) can be rewritten in the following form [37, 38]:

$$\frac{1}{r} \frac{d}{dr} \left(r \frac{d\varphi}{dr} \right) = \frac{2qZc^{bulk}}{\varepsilon \varepsilon_0} \sinh \left(\frac{qZ_i(\varphi - \varphi^{bulk})}{kT} \right) \quad (1.2)$$

Here, the relative permittivity ε is assumed to be constant in the system. This approach was used, for example, by C. L. Rice and R. Whitehead [37] in 1965, which was one of the first works on nanofluidics.

Another common approximation is the Debye-Hückel approximation, where exponential functions in (1.1) are linearized, and consequently the hyperbolic sines in the equations for a symmetric electrolyte (such as eq. (1.2)) are also linearized. Under this assumption, the equation becomes solvable analytically for many practical cases. However, obviously, this approximation does not work if $|\varphi - \varphi^{bulk}| \gtrsim kT/q \approx 0.026 \text{ V}$ (for $T = 300 \text{ K}$). Therefore, it cannot be used in systems with high surface potential (and large surface charge). Fortunately, the general equation (1.1) may be easily solved numerically, and the need in approximations is diminished. However, such approximations are still very convenient for making simple estimations, and tests for numerical simulation correctness.

Generally speaking, PB approach is applicable to many situations, where equilibrium state of charged particles must be modeled, for example, concentrations of electrons and holes in non-degenerate semiconductor. Physics of charge carriers in

semiconductors will be described later in the Chapter 2.

If ionic currents in electrolyte are negligible, Poisson-Boltzmann theory works well for nanodevice simulation [21, 27, 50].

1.2.2 Poisson-Nernst-Planck (PNP) theory

When currents in the modeled system are non-zero, for example due to applied voltage, Nernst-Planck equation must be explicitly solved:

$$\frac{\partial c}{\partial t} = -\nabla \cdot \vec{J}$$

where current density $\vec{J} = -q\mu c \nabla \varphi - qD \nabla c$ has two components: “Drift” and “diffusion”, respectively. Here, μ is mobility, and D is the diffusion coefficient

$$D = \mu \cdot kT / q.$$

Exponential formulas for concentrations that are used in Poisson-Boltzmann method are, in fact, solutions of the Nernst-Planck equation for the system in equilibrium.

In steady state

$$\nabla \cdot \vec{J} = 0$$

Nernst-Planck equation describes the transport of ionic species in a fluid medium, and it must be solved for each of them separately, i.e., to simulate KCl solution, we must solve two equations, for Cl^- , and for K^+ .

For a non-negligible flow of the fluid, ionic current density has one more component induced by the velocity of the fluid [33, 36], and it requires the Navier-Stocks equation, which represents conservation of momentum in the system.

1.2.3 Computer simulations

The PNP approach is widely used to model the ionic transport phenomena in confined spaces such as solid-state nanopores [39, 40] and biological ion channels [41–48].

The validity of the continuum PNP approach for calculating ionic current in the nanopore, has been confirmed for pore radii larger than the Debye length [41]. In [41], the ionic current and conductance were calculated via the PNP model and systematically compared with the results of the Brownian Dynamics simulations of the ionic solution in nanopores with radii varying from 4 Å to 16 Å. A convergence between two theories occurred in pores with radius of ~ 2 Debye lengths. Thus, the continuum approach can be used as long as the ionic strength of the solution is large enough to result in Debye lengths that are smaller than the nanopore radius.

Because Nernst-Planck equations (and Boltzmann statistics) describe both electrolytes and non-degenerate semiconductors, in several papers, solid-state models and semiconductor device simulators are used to model ionic current [47, 48] through nanopores. Such view on the electrolyte also may be found in publications, which use the Poisson-Boltzmann approach [21, 22, 27, 49].

If this similarity between electrolyte and silicon is taken into account, we may introduce a notion of affinity, conduction and valence energy bands, and other properties of solid-state materials in the electrolyte. Though, one should always have to remember that electrons and holes are not ions, there is no recombination of ions, and all newly introduced energy bands and effective densities of states must be eventually converted to properties such as bulk concentration of the solution, surface

potentials of electrodes, and so on.

In our work, we follow this principle, and represent electrolyte as a non-degenerate semiconductor material. This approach lets let us to treat the modeled system as a single heterostructure. Fortunately, an oxide layer always separates silicon material, and solution, therefore, there is no direct contact between ions and electrons and holes. The following chapter provides more details about this representation. And all equations are put together in the Chapter 3, where the complete model is formulated.

Chapter 2

Model of semiconductor heterostructures

Usually semiconductor device models based on the Poisson-Boltzmann approach are quite simple, in case there is only one semiconductor material such as Si [53]¹. However, more detailed treatment is required for heterostructures, which are made of several different materials (with different band gap E_g or electron affinity χ). This is the case in our system, where KCl electrolyte is considered to be just another non-degenerate semiconductor.

The general equations for concentrations of negative and positive charge carriers

¹For a heavily doped degenerate semiconductor, the Fermi-Dirac statistics should be used instead of the Boltzmann's statistics, however, fortunately, the physical approach remains almost the same as in the standard PB approach.

are respectively

$$n = N_C^{\text{eff}} \text{Stat}\left(\frac{E_{Fn} - E_C}{kT}\right), \quad (2.1)$$

$$p = N_V^{\text{eff}} \text{Stat}\left(\frac{E_V - E_{Fp}}{kT}\right), \quad (2.2)$$

where E_V and E_C are energies of the valence and conduction bands, respectively. E_{Fn} and E_{Fp} are quasi-Fermi energies for negative and positive charge carriers.

In (2.1) and (2.2), $\text{Stat}(\eta)$ stands for corresponding statistics. In non-degenerate semiconductor, $\text{Stat}(\eta) = \exp(\eta)$, and it yields Boltzmann statistics. In degenerate semiconductor, $\text{Stat}(\eta) = \mathcal{F}_{1/2}(\eta)$, which is the Fermi-Dirac integral [54]. In our model, the latter is used for the heavily doped solid-state membrane, and the former describes ionic concentrations in the electrolyte, or any semiconductor with low doping.

In semiconductor, where n and p correspond to electron and hole concentrations, the effective density of states at the conduction and valence band edges are

$$N_C^{\text{eff}} = 2 \left(\frac{2\pi m_n^* kT}{h^2} \right)^{3/2}$$

$$N_V^{\text{eff}} = 2 \left(\frac{2\pi m_p^* kT}{h^2} \right)^{3/2},$$

where m_n^* and m_p^* are effective masses of electrons and holes.

In KCl electrolyte, negative the charge carriers are Cl^- , and the positive charge carriers are K^+ ions. Thus, constants N_C^{eff} and N_V^{eff} can be determined by solving equations $n = [\text{KCl}]_0$ and $p = [\text{KCl}]_0$ in the *bulk* solution, which guarantees the electrical neutrality on the electrolyte. Also, it will be shown below, how energy levels E_C , E_V , E_{Fn} , and E_{Fp} may be represented in terms of electric potential and applied voltage, which have explicit meaning in the electrolyte.

The following discussion is mostly presented in terms of solid-state semiconductors, though, it may be directly applied to electrolyte materials. Remarks are added, where necessary.

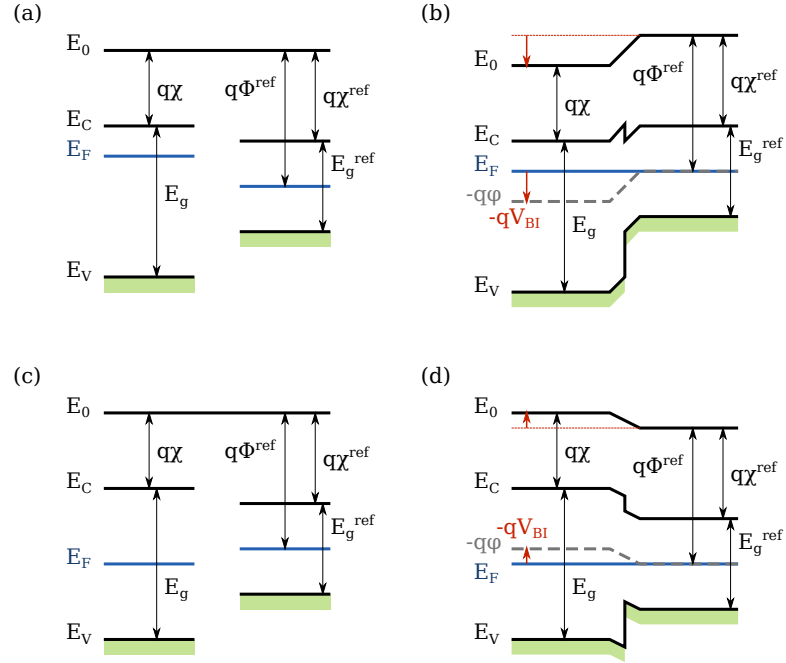


Figure 2.1: Heterojunctions (unbiased). The reference intrinsic semiconductor is shown on the right side of each junction. (a) \rightarrow (b): Left semiconductor is not intrinsic. (c) \rightarrow (d): Left semiconductor is intrinsic.

Since n and p concentrations (2.1, 2.2) are functions of the differences between energy levels, it is a common practice [56](p.28) [57] to set a zero energy-level such that quasi-Fermi energies are zero in equilibrium (situation, when no external forces are applied). In this case, it is convenient to define quasi-Fermi potentials ψ_n and ψ_p , such that $E_{Fn} = -q\psi_n$ and $E_{Fp} = -q\psi_p$.

The effective conduction and valence band energies are

$$E_C = E_0 - q\chi$$

$$E_V = E_C - E_g = E_0 - q\chi - E_g,$$

where E_0 is the vacuum energy level (see Figure 2.1), and χ is the electron affinity of the material. In its turn,

$$E_0 = -q\varphi + \text{const, where } \varphi \text{ is the electric potential.} \quad (2.3)$$

The constant provides freedom to choose a convenient zero-level of the potential φ . It is common [57](p. 10) to consider a reference material that is intrinsic (i.e. $n = p = n_i$ in equilibrium), and has $\varphi = 0$. Then, the vacuum level in the reference material is simply

$$E_0^{\text{ref}} \equiv E_F + q\Phi^{\text{ref}} = q\Phi^{\text{ref}} = \frac{E_g^{\text{ref}}}{2} + q\chi^{\text{ref}},$$

$$E_C^{\text{ref}} = \frac{E_g^{\text{ref}}}{2}, \text{ and } E_V^{\text{ref}} = -\frac{E_g^{\text{ref}}}{2}.$$

$q\Phi^{\text{ref}}$ is called the *work function*, and it is the difference between the vacuum level and the Fermi level. Here we have taken into account that quasi-Fermi-potentials are zero in equilibrium.

Then, all energy levels in real materials may be referenced to this material. In our model *intrinsic silicon* is used as such material.

Non-intrinsic Si (homojunction with the reference material). All energy bands of doped (non-intrinsic) silicon are shifted by $-q\varphi$, which may be non-zero due to doping (and then it is called “built-in” or “bulk” potential) or applied voltage:

$$E_0^{\text{Si}} = \frac{E_g^{\text{ref}}}{2} + q\chi^{\text{ref}} - q\varphi,$$

$$E_C^{\text{Si}} = \frac{E_g^{\text{ref}}}{2} - q\varphi, \text{ and } E_V^{\text{Si}} = -\frac{E_g^{\text{ref}}}{2} - q\varphi.$$

Here, we assume that the band gap and affinity do not change with increase in doping, in other words, $E_g^{\text{Si}} = E_g^{\text{ref}}$ and $\chi^{\text{Si}} = \chi^{\text{ref}}$. However it is not exactly true, and a proper correction may improve the model.

Therefore, the concentrations are:

$$n^{\text{Si}} = N_C^{\text{eff}} \mathcal{F}_{1/2} \left[\frac{q(\varphi - \psi_n) - \frac{E_g^{\text{ref}}}{2}}{kT} \right] \quad (2.4)$$

$$p^{\text{Si}} = N_V^{\text{eff}} \mathcal{F}_{1/2} \left[\frac{-q(\varphi - \psi_p) - \frac{E_g^{\text{ref}}}{2}}{kT} \right] \quad (2.5)$$

The difference between two quasi-Fermi potentials ψ_n and ψ_p must be taken into account, if there is a non-negligible current flowing through the junctions in the modeled system, where the Fermi-level effectively “splits”. Our simulations are usually made for a single layer of doped silicon, or p-n junction membranes with forward bias less than the junction built-in potential, which means that the depletion layer is still present in the junction. In this case, the quasi-Fermi potentials can be assumed to be *constant* in silicon, and both are equal to the applied voltage:

$$\psi_n = \psi_p = V \quad (2.6)$$

These bulk built-in potentials can be obtained from the condition of electroneutrality $n^{\text{Si}} = N_D^+$ for n-doped Si (neglecting p^{Si} and N_A^-), and $p^{\text{Si}} = N_A^-$ for p-doped Si (neglecting n^{Si} and N_D^+):

$$V_{BI,n} - \psi_n = \mathcal{F}_{1/2}^{-1}(N_D^+/N_C^{\text{eff}})kT/q + E_g^{\text{ref}}/2q$$

$$V_{BI,p} - \psi_p = -\mathcal{F}_{1/2}^{-1}(N_A^-/N_V^{\text{eff}})kT/q - E_g^{\text{ref}}/2q$$

In a non-degenerate semiconductor, the inverse Fermi-integral may be replaced with the natural logarithm. Actually, in our model, these equations are not needed for simulation: Because of the presence of dopant atoms, the self-consistent solution of Poisson’s equation ensures the electroneutrality of the bulk, and simulations converge to these levels of potential. However, these formulas can be used as initial

guess for potential:

$$\varphi = V_{BI,n} + V \text{ for n-Si, or } \varphi = V_{BI,p} + V \text{ for p-Si.} \quad (2.7)$$

If we have two layers of n- and p-doped silicon, which form a p-n junction, the so-called built-in potential of the junction is equal to the difference ($V_{BI,n} - V_{BI,p}$).

General case. Anderson's rule [57](p. 9) provides a method to construct a band diagram of a heterojunction. It is based on a principle that the vacuum energy level E_0 must be continuous, then $E_C = E_0 - q\chi$ and $E_V = E_0 - q\chi - E_g$. Since χ and E_g are different on two sides of the heterojunction, conduction and valence bands have discontinuities, and $(E_C - E_C^{\text{ref}})$ and $(E_V - E_V^{\text{ref}})$ may be expressed as follows (also see Figure 2.1):

$$E_C - E_C^{\text{ref}} = q\chi^{\text{ref}} - q\chi$$

$$E_V - E_V^{\text{ref}} = E_g^{\text{ref}} - E_g + q\chi^{\text{ref}} - q\chi$$

Intrinsic heterojunction. Using Anderson's rule, concentration of charge carriers in arbitrary intrinsic semiconductor material with respect to the reference material can be represented:

$$n = N_C^{\text{eff}} \mathcal{F}_{1/2} \left[\frac{q(\varphi - \psi) - \frac{E_g}{2} + \left[\frac{E_g}{2} - \frac{E_g^{\text{ref}}}{2} + q(\chi - \chi^{\text{ref}}) \right]}{kT} \right] \quad (2.8)$$

$$p = N_V^{\text{eff}} \mathcal{F}_{1/2} \left[\frac{-q(\varphi - \psi) - \frac{E_g}{2} - \left[\frac{E_g}{2} - \frac{E_g^{\text{ref}}}{2} + q(\chi - \chi^{\text{ref}}) \right]}{kT} \right] \quad (2.9)$$

The built-in (equilibrium) potential in the material is

$$V_{BI} = -\frac{1}{q} \left[\frac{E_g}{2} - \frac{E_g^{\text{ref}}}{2} + q(\chi - \chi^{\text{ref}}) \right] \quad (2.10)$$

This potential corresponds to the total band bending (as shown in Figure 2.1 ($c \rightarrow d$))

We use this equations to calculate concentrations of ions in KCl solution in the electrostatic problem. However, instead of Fermi-integrals $\mathcal{F}_{1/2}(\eta)$, the Boltzmann statistics must be used (see equations (3.4) and (3.5)). Note, that in the electrostatic problem, the quasi-Fermi potentials $\psi = 0$ in KCl.

When the Nernst-Planck equations are solved to find ionic concentrations, equations (2.8) and (2.9) are not needed, however the built-in potential V_{BI} is still required for the boundary conditions for φ .

Assuming ohmic boundary condition [57](p.53), for a biased semiconductor in a heterostructure with applied voltage V (with respect to the reference material) the boundary conditions for the electric potential and the quasi-Fermi potentials are

$$\varphi = V_{BI} + V \quad (2.11)$$

$$\psi_n = \psi_p = V \quad (2.12)$$

Note, that similar equations (2.6 and 2.7) are provided in the paragraph about non-intrinsic Si. However, these equations play different roles in these two cases. When Nernst-Planck equations are used to calculate concentrations, (2.11) define boundary conditions. Whereas in non-intrinsic Si, (2.7) can be used as initial guess for the electric potential in the whole volume, and (2.6) defines quasi-Fermi potentials also in the whole volume of the semiconductor (it is possible, because electric currents in Si layers are assumed to be negligible in the steady state).

Chapter 3

Physical model

3.1 Membrane composition

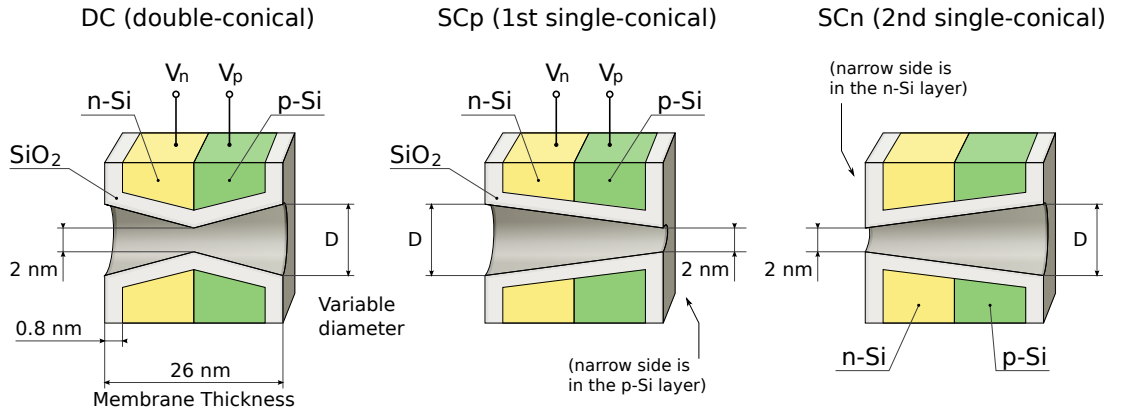


Figure 3.1: Modeled geometries of the pore: (Left) symmetric double-conical nanopore; (Center) and (Right) are single-conical geometries with a narrow side in the p-Si layer or n-Si layer, respectively. Width of the membrane is 26 nm, thickness of the SiO₂ coating is 0.8 nm. Membrane separates two compartments with KCl solution. V_n and V_p are voltages, which are applied to corresponding silicon layers.

In our work, we modeled several membrane compositions and nanopore geometries. However, most of the results were obtained for a semiconductor membrane

that consists of two layers of n- and p- heavily-doped Si. The membrane is immersed into fully dissociated KCl electrolyte with concentration $[KCl]_0 = 0.1 \text{ M}$. Three analyzed pore geometries are shown in Figure 3.1, one symmetric double-conical and two single-conical configurations.

Such membrane structure had been proposed in previous publications [16, 17, 21, 22], and it has the following advantages:

- Semiconductor layers with applied voltages V_n and V_p work as gates, controlling potential in the pore.
- p-n junction produces high gradient of the electric potential inside the pore.
- Two silicon layers make system more versatile than only one.

The system is characterized by the following variables:

- φ , electric potential;
- n and p , concentrations of electrons and holes in silicon;
- $[Cl^-]$ and $[K^+]$, concentrations of ions in KCl solution.

Note that it is possible to choose a different set of variables. Several alternatives exist, for example, concentrations may be replaced by corresponding quasi-Fermi-potentials. (see [56] (“Dependent Variables”, p. 134) and [36] (“Logarithmic Transform of the Nernst-Planck Equations”, p. 258) for details). Such alternatives have some advantages as well as disadvantages. However, for the general case, our choice may be considered optimal.

3.2 Mathematical formulation of the problem

In this section, we summarize the previously described theory, and formulate the mathematical problem in the form of a boundary value problem.

3.2.1 Poisson's equation

The electric potential φ is determined from the solution of Poisson's equation:

$$\nabla(\varepsilon \nabla \varphi) = -\frac{\rho}{\varepsilon_0}, \text{ where} \quad (3.1)$$

$$\rho = q(-n + p - N_A^- + N_D^+ + N_{\text{surf}} - [Cl^-] + [K^+]).$$

ε is the relative permittivity, N_{surf} is the equivalent volumetric concentration of the oxide surface charge (σ_{surf}) on the boundary with $[KCl]$.

3.2.2 Concentrations of electrons and holes in silicon

In silicon, concentrations of electrons n and holes p are calculated using equations (2.4) and (2.5):

$$n = N_C^{\text{eff}} \mathcal{F}_{1/2} \left(\frac{q(\varphi - V) - \frac{E_g^{\text{Si}}}{2}}{kT} \right), \quad (3.2)$$

$$p = N_V^{\text{eff}} \mathcal{F}_{1/2} \left(\frac{-q(\varphi - V) - \frac{E_g^{\text{Si}}}{2}}{kT} \right), \text{ where} \quad (3.3)$$

$$N_C^{\text{eff}} = 2 \left(\frac{2\pi m_n^* kT}{h^2} \right)^{3/2}, \quad N_V^{\text{eff}} = 2 \left(\frac{2\pi m_p^* kT}{h^2} \right)^{3/2}.$$

m_n^* and m_p^* are effective masses of electrons and holes. N_A^- , N_D^+ are concentrations of dopant atoms. E_g^{Si} is the band gap in Si. The voltage $V = V_n$ in the n-Si layer, and it is equal to V_p in the p-Si layer, as shown in Figure 3.2.

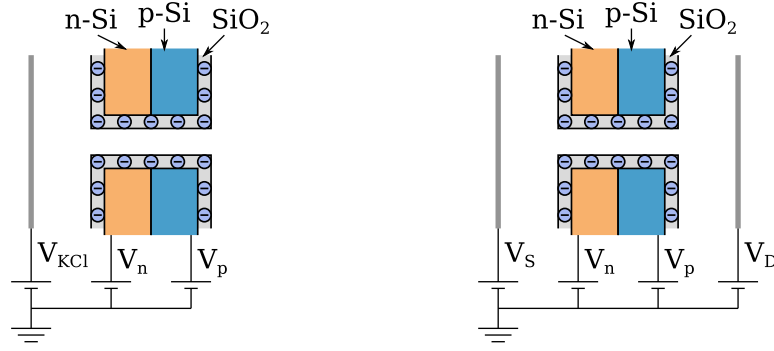


Figure 3.2: Schematic representation of applied voltages V . (Left) Electrostatic case. Voltage V_{KCL} defines potential in the whole electrolyte. (Right) Nernst-Planck case. V_S and V_D are different in two compartments. In both situations, V_n and V_p are applied to silicon layers.

3.2.3 Concentrations of ions

Generally, to find $[Cl^-]$ and $[K^+]$, we have to solve Nernst-Planck equations. However, in absence of ionic current, the solution is already known: $[Cl^-]$ and $[K^+]$ are governed by the Boltzmann statistics. This electrostatic problem is formulated below in the Method I.

When current is non-zero, the Nernst-Planck equations must be solved, they are described in the Method II.

Method I. Electrostatic solution (Boltzmann).

Using equations for charge carriers in intrinsic semiconductor in heterostructure (2.8) and (2.9):

$$[Cl^-] = N_{C,[Cl^-]}^{\text{eff}} \exp \left(\frac{q(\varphi - V) - \frac{E_g^{\text{KCl}}}{2} - qV_{BI}^{\text{KCl}}}{kT} \right) \quad (3.4)$$

$$[K^+] = N_{V,[K^+]}^{\text{eff}} \exp \left(\frac{-q(\varphi - V) - \frac{E_g^{\text{KCl}}}{2} + qV_{BI}^{\text{KCl}}}{kT} \right) \quad (3.5)$$

The built-in (equilibrium) potential of the electrolyte is

$$V_{BI}^{KCl} = -\frac{1}{q} \left[\frac{E_g^{KCl}}{2} - \frac{E_g^{Si}}{2} + q(\chi^{KCl} - \chi^{Si}) \right] \quad (3.6)$$

Electric potential in bulk electrolyte is $\varphi = V + V_{BI}^{KCl}$, Therefore, constants $N_{C, [Cl^-]}^{eff}$ and $N_{V, [K^+]}^{eff}$ must be equal, and can be determined from the bulk concentration of KCl:

$$N_{C, [Cl^-]}^{eff} = N_{V, [K^+]}^{eff} = [KCl]_0 \exp \left(\frac{E_g^{KCl}/2}{kT} \right)$$

We obtain the standard Boltzmann statistics:

$$[Cl^-] = [KCl]_0 \exp \left(\frac{q(\varphi - V - V_{BI}^{KCl})}{kT} \right) \quad (3.7)$$

$$[K^+] = [KCl]_0 \exp \left(\frac{-q(\varphi - V - V_{BI}^{KCl})}{kT} \right) \quad (3.8)$$

The electrostatic solution works only for constant voltage $V = V_{KCl}$ applied to the whole KCl volume (Figure 3.2 (Left)). Otherwise, in the presence of voltage applied across the membrane ($V_S \neq V_D$, as shown in Figure 3.2 (Right)), the Nernst-Planck equations must be solved explicitly (here, subscripts “S” and “D” stand for “source” and “drain”).

Method II. Ionic current (Nernst-Planck equation).

Steady state Nernst-Planck equations for ionic current densities:

$$\nabla \cdot \vec{J} = 0$$

Current densities are

$$\vec{J}_{Cl} = -q\mu[Cl^-]\nabla\varphi + qD\nabla[Cl^-],$$

$$\vec{J}_K = -q\mu[K^+]\nabla\varphi - qD\nabla[K^+].$$

The resulting equations for $[Cl^-]$ and $[K^+]$ are

$$\nabla \cdot (-\mu[Cl^-]\nabla\varphi + D\nabla[Cl^-]) = 0,$$

$$\nabla \cdot (-\mu[K^+]\nabla\varphi - D\nabla[K^+]) = 0.$$

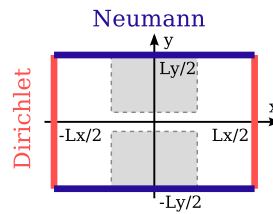
Discretization of the Nernst-Planck equations is an important and not a trivial topic, compared to discretization of the Poisson's equation, we describe this question in detail in Chapter 5.

3.2.4 Boundary Conditions

Introducing a reference frame such that axis X is the axis of the pore, and axes Y and Z are parallel to the plane of the membrane, the boundary conditions may be defined in the following way:

For potential:

$$\begin{aligned} \varphi|_{x=-L_x/2} &= V_S + V_{BI}^{KCl}, \\ \varphi|_{x=L_x/2} &= V_D + V_{BI}^{KCl}, \\ \frac{\varphi}{dy}\Big|_{y=\pm L_y/2} &= \frac{\varphi}{dz}\Big|_{z=\pm L_z/2} = 0. \end{aligned}$$



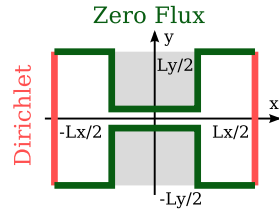
For ionic concentrations:

$$c|_{x=\pm L_x/2} = [KCl]_0,$$

$$(\vec{J} \cdot \hat{j})|_{y=\pm L_y/2} = 0,$$

$$(\vec{J} \cdot \hat{k})|_{z=\pm L_z/2} = 0,$$

$$(\vec{J} \cdot \hat{n})|_{\delta\Gamma} = 0,$$



where $\delta\Gamma$ is the surface of the membrane, and \hat{n} is the normal to it.

Chapter 4

Electrostatic problem

4.1 Introduction

In this chapter, we give analysis of the electric potential profiles in the pore. We provide estimated I-V curves and demonstrate dependence between the current rectification ratio and the variation of the potential in the nanopore, $\Delta\varphi = \varphi_n - \varphi_p$, where φ_n and φ_p are two potentials from the central axis of the pore as shown in Figure 4.2. The last part is devoted to $\Delta\varphi$ itself. Comparisons of geometries are provided throughout the text, as well as the effects of voltages applied to silicon layers. We try to give a systematic comparison of different nanopore geometries, and evaluate our ability to control their properties.

4.1.1 Model

Here, we use the electrostatic model described in the previous chapter, which includes:

1. Poisson's Equation (3.1),
2. Fermi-Dirac statistics for electrons (3.2) and holes (3.3),
3. Boltzmann Statistics for $[Cl^-]$ (3.7) and $[K^+]$ (3.8).
4. Boundary conditions for φ (Section 3.2.4).

4.1.2 Computational method

Numerical simulations are performed on a uniform, cubic, three-dimensional grid consisting of $161 \times 81 \times 81$ grid points with the size of the grid spacing equal to 0.4 nm. Thus, the size of the simulated volume is $64.4 \times 32.4 \times 32.4 \text{ nm}^3$. The reduction of the grid spacing to 0.2 nm leads to the difference of $\sim 2 \text{ mV}$ for the average potential in the nanopore vicinity which is about 2% of the total potential variation in the pore. Our choice of grid spacing allows for fast computation without significantly sacrificing the precision. Various material constants and simulation parameters are listed in Table 4.1.

Poisson's equation is solved iteratively until the self-consistent solution is reached. The Gummel's method [56] (p. 211) is used to accelerate convergence. To solve it for the potential $\varphi(\vec{r})$, the equation 3.1 is first linearized. The linearized differential equation is solved using an implicit finite difference method [58] that gives a system

of linear equations. The iteration process is repeated until the relative difference in the potential values between two consecutive iterations does not exceed 10^{-7} . More detailed description of the iteration process is provided in the Section 5.2.

4.1.3 Nanopore geometries and membrane biases

We consider three nanopore geometries illustrated in Figure 3.1: Symmetric double-conical (DC), single-conical with the narrow opening in the *p*-Si layer (SCp), and single-conical with the narrow opening in the *n*-Si layer (SCn).

In single-conical geometries, the larger opening of the pore has the diameter denoted by D that we vary between 2 nm and 10 nm. The smaller diameter of the pore is always fixed at 2 nm. In the double-conical geometry, both outer diameters are equal to D and are varied while the center diameter fixed at 2 nm. The value of $D = 2$ nm makes all three geometries (DC, SCp and SCn) cylindrical and identical.

We study a range of membrane voltage biases between -0.8 V and 0.8 V applied to the *n*-Si and *p*-Si layers, and denoted V_n and V_p , respectively. Throughout the work, we follow a color scheme in which data pertaining to the DC pore with $D = 10$ nm are drawn in blue, data for the SCp pore with the same D are in green, and data for the SCn pore are in red color. The common cylindrical case ($D = 2$ nm) is shown in black color. The data for all other shapes with intermediate diameters are shown in color variations between black and blue/green/red for DC, SCp, and SCn geometries, respectively.

4.2 Results and discussion

4.2.1 Electrostatic potential and ionic concentration

The calculated electric potential through the center of the double-conical pore (DC) is shown in Figure 4.1. Two distinct membrane biases with $V_n = -0.8$ V [Figure 4.1A] and $V_n = 0.8$ V [Figure 4.1 (B)] are considered with $V_p = 0$ V in both situations. The former produces negative potential in the pore on both sides of the membrane and the latter results in positive potential on the n -Si side of the membrane and negative potential on the p -Si side of the membrane inside the pore. Due to the presence of negative static charge on the surface of the nanopore, V_n has a stronger effect on the potential compared to V_p (results are not shown). In general, we find that large negative biases ($V_n \lesssim -0.8$ V) applied to the n -Si layer have similar effects on the potential in the pore as described above for the specific case of $V_n = -0.8$ V.

According to equations (3.7) and (3.8), negatively charged Cl^- ions have a high concentration ($[\text{Cl}^-] > [\text{KCl}]_0$) in the regions with positive potential, and a low concentration ($[\text{Cl}^-] < [\text{KCl}]_0$) in regions with negative potential. Positively charged K^+ ions follow an opposite trend with $[\text{K}^+] < [\text{KCl}]_0$ for positive potential, and $[\text{K}^+] > [\text{KCl}]_0$ for negative potential. This is demonstrated in Figs. 4.1(B and D) where $[\text{K}^+]$ and $[\text{Cl}^-]$ concentrations are shown for the DC geometry ($D = 6$ nm). The resulting variation in ionic concentrations is between $0.02 \times [\text{KCl}]_0$ and $50 \times [\text{KCl}]_0$.

The potential profiles for single-conical pores are shown in Figure 4.2(A-D). The

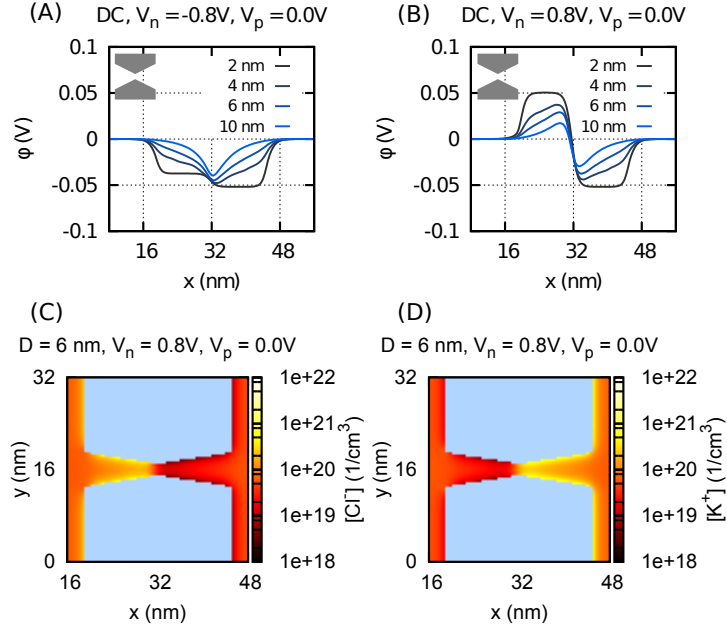


Figure 4.1: (A) and (B): Profiles of the electrostatic potential ϕ in the double-conical pore for $D = 2$ nm, 4 nm, 6 nm, and 10 nm. In (A), the membrane bias is $V_n = -0.8$ V while in (B), $V_n = 0.8$ V. $V_p = 0$ V in both cases. (C) and (D): Cross sections of the ionic concentrations through the center of the DC pore with $D = 6$ nm and $(V_n, V_p) = (0.8, 0)$ V.

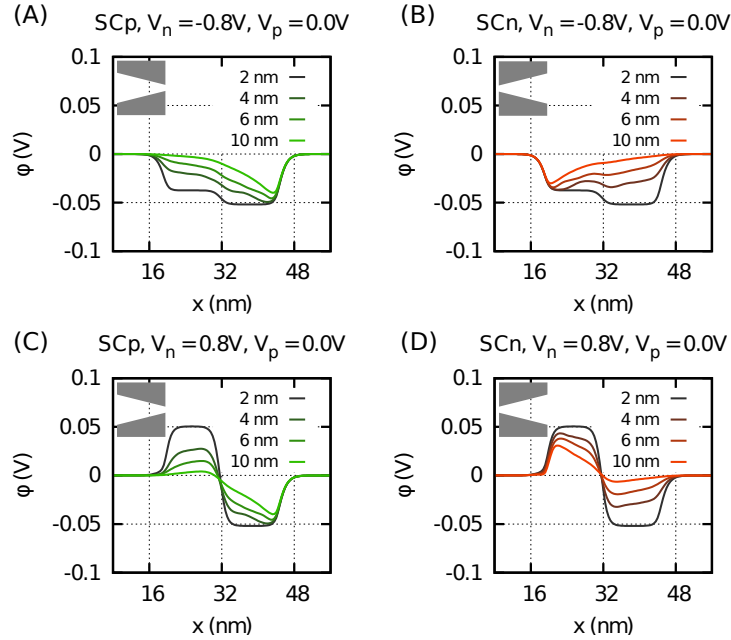


Figure 4.2: Profiles of the electrostatic potential $\phi(\vec{r})$ through the center of the pore for two single-conical pores. In (A) and (C), the membrane bias is $V_n = -0.8$ V; in (B) and (D), $V_n = 0.8$ V. $V_p = 0$ V in both cases. In (A) and (C) [(B) and (D)], the potentials are shown for the SCp (SCn) geometry.

membrane bias voltages V_n and V_p are the same as for the double-conical nanopore shown in Figure 4.1. In Figs. 4.1 and 4.2, the common case of cylindrical nanopore geometry is shown by black curves. We observe that for large pore diameters D , $\varphi(\vec{r}) \approx 0$ at the wide end of the pore, and $|\varphi(\vec{r})|$ is the largest at its narrow end. This is why V_n , when applied to the narrow end of the SCn pore affects the potential much stronger than V_n in the SCp nanopore where it is applied to the wide end (cf. curves for diameter $D = 10 \text{ nm}$ in Figure 4.2 (B) and (D) (red color) with curves that correspond to the same diameter in Figure 4.2 (A) and (C) (green color)). This effect is described in more detail below, see the discussion for Figure 4.4. Comparison of V_n and V_p in terms of their ability to control potential distribution is also provided there.

4.2.2 Characterization of the electrostatic potential in the nanopore

We now perform a general characterization of the potential distribution in the nanopore. For this purpose we record two values of the potential φ_i , $i = n, p$, inside the nanopore near the centers of n -Si and p -Si layers, $\varphi_n = \varphi(x = 26 \text{ nm})$ (marked by solid square) and $\varphi_p = \varphi(x = 38 \text{ nm})$ (marked by an open square), respectively, see Figure 4.3(A&B). Thus, the value of φ_n is mostly affected by V_n while the influence of V_p is minimized. Similarly, φ_p is controlled by V_p and it depends weakly on V_n . Also, we found that φ_n and φ_p potentials are close to the average potentials on the n -Si and p -Si sides of the pore, respectively.

Cylindrical nanopore. Due to the presence of the dopant ions, the n -Si side of the membrane has a positively charged depletion layer, whereas the p -Si side of the

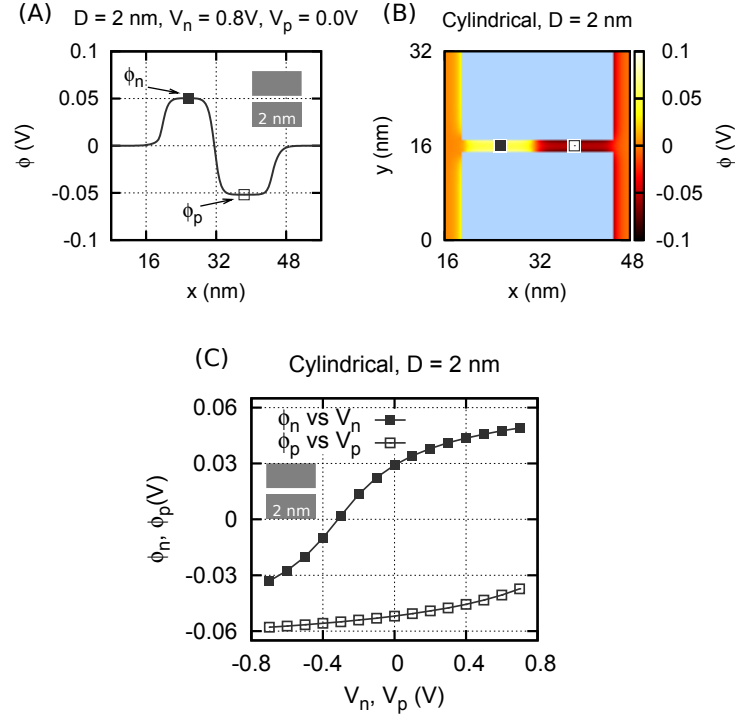


Figure 4.3: (A) The profiles of the electric potential for the cylindrical nanopore ($D = 2$ nm).

Potentials φ_n and φ_p are marked by solid (■) and open (□) squares, respectively. (B) The cross section of the electrostatic potential $\varphi(\vec{r})$ for the same pore with two representative potentials φ_n and φ_p marked as in (A). (C) The potential φ_n as a function of the applied membrane bias voltage V_n ($V_p = 0$), and φ_p as a function of V_p ($V_n = 0$).

membrane has a negatively charged depletion layer near the membrane surface. Since surface oxide layer (SiO_2) is negatively charged, it effectively negates positively charged depletion layer on the n -Si side, while enhancing negatively charged depletion layer on the p -Si side. Thus, when no membrane bias is applied, there is an excess of K^+ ions in the pore on the p -Si side of the membrane, while no excess ions are accumulated on the n -Si side of the membrane. High concentration of potassium ions screens the electrostatic potential in the pore and makes it difficult to control p -Si side of the pore with applied membrane bias, as shown below. To demonstrate this, we plot φ_n as a function of the applied membrane bias voltage V_n (keeping $V_p = 0$) and φ_p as a function of V_p ($V_n = 0$), see Figure 4.3C. We observe

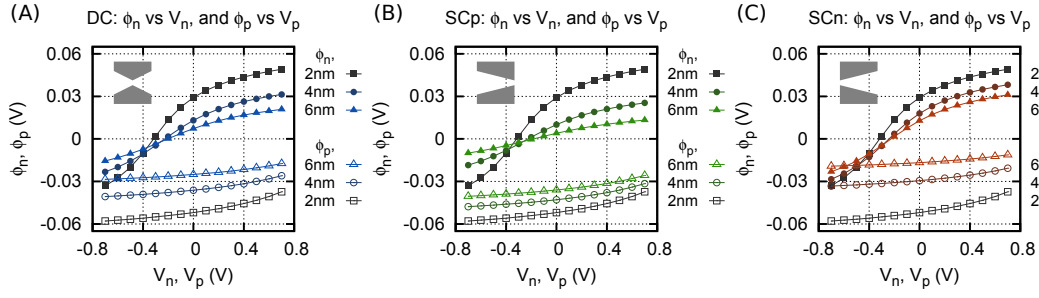


Figure 4.4: The electrostatic potentials φ_n and φ_p as functions of the applied membrane bias voltage V_n ($V_p = 0$) and V_p ($V_n = 0$) for different nanopore diameters D : (A) Double-conical nanopore (DC); (B) Single-conical nanopore with the smaller diameter on the p -Si side (SCp); (C) Single-conical nanopore with the smaller diameter on the n -Si side (SCn).

that the value of φ_n on the n -Si side rises quickly by about 80 mV while φ_p on the p -Si side grows more slowly by less than 25 mV over the same range of applied membrane biases.

Non-cylindrical nanopores. In Figure 4.4(A-C) potentials φ_n vs. V_n (with $V_p = 0$) and φ_p vs. V_p (with $V_n = 0$) for the non-cylindrical nanopore geometries with $D = 4$ nm and 6 nm are shown. We also show potentials φ_p and φ_n , calculated for the cylindrical nanopore for reference purposes (black curves). We summarize the features found in Figure 4.4 as follows.

First we notice that the increase in the nanopore diameter D always leads to the shrinkage of the available potential range for all three nanopore geometries, cf. curves with triangles ($D = 6$ nm) with curves with squares ($D = 2$ nm) in Figs. 4.4(A, B and C). This is because the increase in D effectively positions the membrane further from the nanopore's center axis and therefore allows for greater screening by the electrolyte solution. As a result, the electrostatic potential become less sensitive to the applied membrane bias. In addition, due to the negative surface charge,

the potential φ_n on the n -Si side of the membrane is more sensitive to the applied bias voltage for all three geometries. At the same time, the variation of φ_p is restricted to about 10-15 mV, similar to what was found for the cylindrical nanopore (Figure 4.3C), see the three bottom curves in Figure 4.4(A-C).

Furthermore, out of all considered nanopore geometries besides the cylindrical case, it is the SCn nanopore, which has the smaller opening on the n -Si side of the membrane, that exhibits a wider range of accessible potentials, and thus, it is better suited for tunable control over ionic current flowing through the nanopore, which is further demonstrated in Section 4.2.3. Finally, it is possible that this nanopore (SCn) will also be better suited to control translocation of a large molecule permeating through the nanopore.

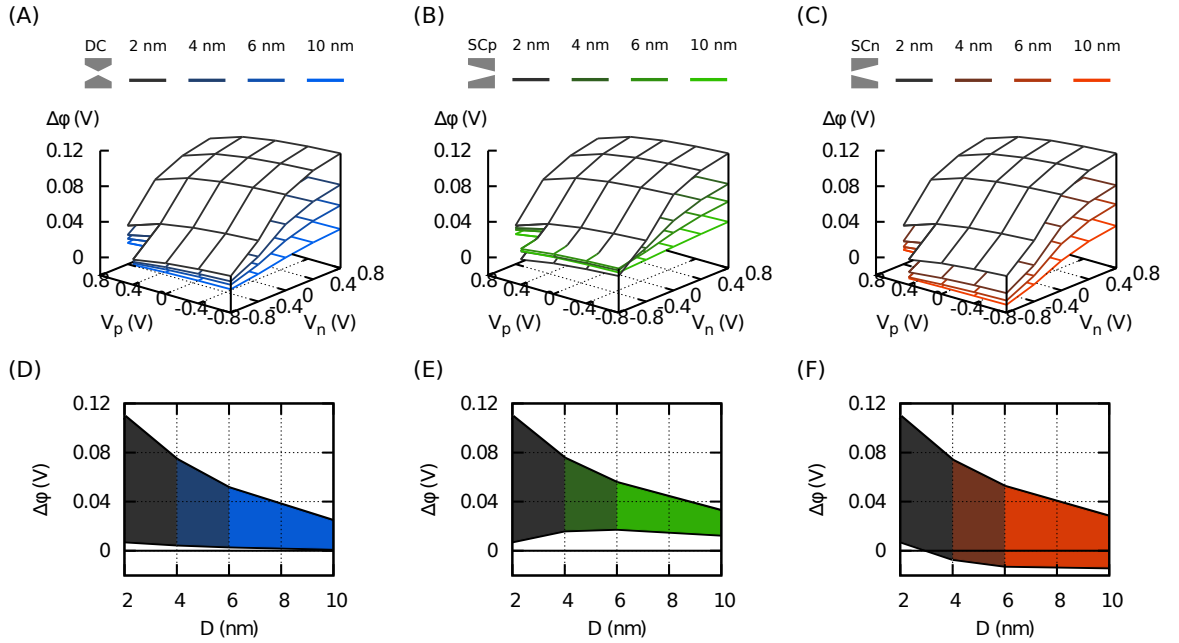


Figure 4.5: The range of accessible potential differences $\Delta\phi$ obtained by varying V_n and V_p from -0.8 V to 0.8 V plotted as a function of D for different nanopore geometries: (A) DC, (B) SCp and (C) SCn.

If we vary both membrane bias voltages (V_n and V_p), we obtain a continuous range

of potential differences $\Delta\varphi = \varphi_n - \varphi_p$ available for each structure, see Figure 4.5. We can tune the applied membrane biases to obtain any specific potential difference $\Delta\varphi$ in the pore, within the available range. A particular value of $\Delta\varphi$ is closely related to a particular regime of ion filtering through the pore. For example, a large potential difference $\Delta\varphi$ results in a diode-like ionic current-voltage characteristic with a large rectification ratio, as shown in the next section. Similarly, $\Delta\varphi$ is also important for controlling biomolecule translocation through the pore. Larger $\Delta\varphi$ means that there is a larger electric field and stronger force applied to a charged molecule. As such, we are interested in the nanopore membranes with the largest range of $\Delta\varphi$ values, and according to Figure 4.5, these are the cylindrical nanopore and the single-conical nanopore with the smaller opening on the n -Si side of the membrane (SCn).

4.2.3 Ionic current-voltage characteristics and rectification ratios

We use a model previously described in papers [21, 22, 51] to estimate the ionic current I through the pore vs. external electrolyte bias V , at constant membrane voltage bias. In this model we assume that the ionic fluxes are governed by the Nernst-Planck equation with contributions from ion diffusion and drift. The total ionic current through the nanopore is given by the sum of the fluxes for all ionic species. In calculations of ionic fluxes, we use the electrostatic potential which is the sum of the equilibrium self-consistent potential obtained from the solution of Poisson's equation (3.1) and the potential due to the electrolyte bias V (V is assumed

to drop linearly across the membrane).

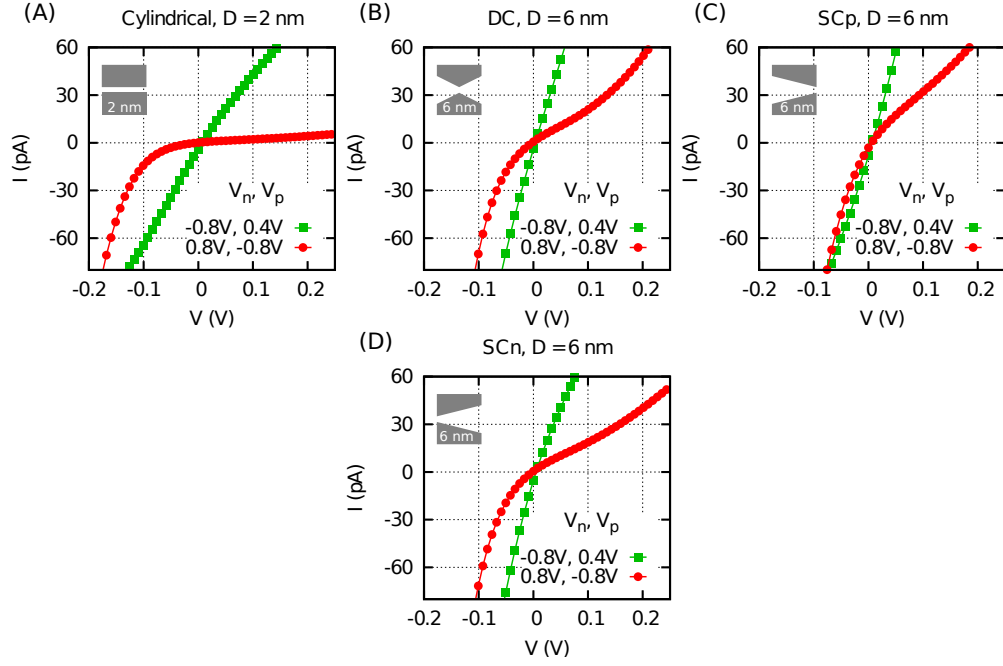


Figure 4.6: Ionic current-voltage characteristics for different nanopore geometries: (A) Cylindrical pore; (B) Double-conical pore with $D = 6$ nm; (C) and (D) Single-conical pores SCp and SCn, respectively, with $D = 6$ nm. The semiconductor membrane for each nanopore geometry was biased with $(V_n, V_p) = (-0.8, 0.4)$ V (green squares), and $(V_n, V_p) = (0.8, -0.8)$ V (red circles).

The ionic current-voltage characteristics that we obtained using this approach are shown in Figure 4.6 for different nanopore geometries. All subplots in Figure 4.6 contain two current-voltage characteristics calculated for (1) $(V_n, V_p) = (-0.8, 0.4)$ V (green squares), and (2) $(V_n, V_p) = (0.8, -0.8)$ V (red circles). In case (1), membrane biases result in almost ohmic linear current-voltage characteristic whereas I-V curves in the second case exhibits non-linear diode-like characteristics. By varying the applied membrane biases V_n and V_p between -0.8 V and 0.4 V, we were also able to obtain ionic current-voltage characteristics that fall in between two curves in Figure 4.6 for each nanopore geometry (not shown).

We calculated the rectification ratio RR for each current-voltage curve as a ratio of

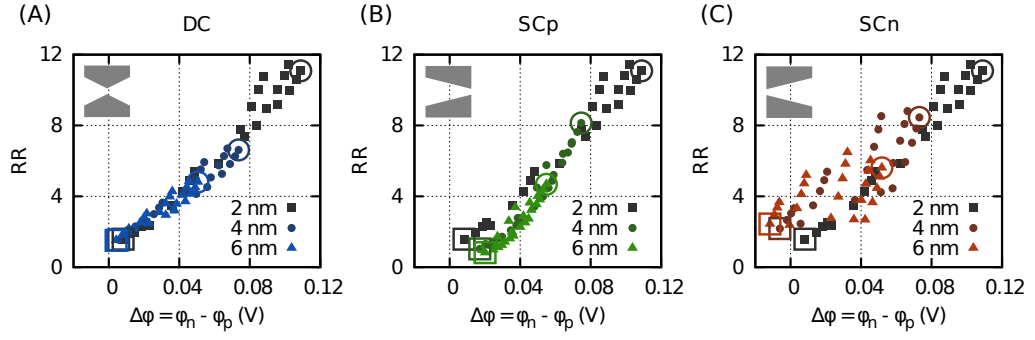


Figure 4.7: Current rectification ratio RR as a function of the electrostatic potential variation in the pore $\Delta\varphi$ for different nanopore geometries: (A) DC pore; (B) SCp pore; (C) SCn pore. Each plot includes three families of data points: solid squares are for $D = 2$ nm, solid circles are for $D = 4$ nm, and solid triangles are for $D = 6$ nm. Each data set was obtained by varying V_n and V_p from -0.8 V to 0.4 V. Large open circles mark membranes biased with $(V_n, V_p) = (0.8, -0.8)$ V for which $\Delta\varphi$ is maximal. Open squares correspond to $(V_n, V_p) = (-0.8, 0.4)$ V when $\Delta\varphi$ is minimal.

ionic currents at $|V_0| = 0.12$ V: $RR = I(-V_0)/I(V_0)$. In Figure 4.7, the rectification ratios as a function of the potential variation in the pore are shown for all considered nanopore geometries. We find that the rectification ratio depends on the variation of the electrostatic potential in the nanopore $\Delta\varphi = \varphi_n - \varphi_p$, and for all nanopore geometries this dependence is close to linear. Thus, high values of RR are found for membranes with large $\Delta\varphi$ with diode-like $I - V$ characteristics while small RR 's are obtained for membranes with small $\Delta\varphi$ and linear (ohmic) current dependencies. We see that the degree of current rectification varies among nanopore geometries. For cylindrical nanopore [Figure 4.6A] the rectification ratios are the greatest (maximum $RR \sim 12$). For non-cylindrical nanopores with the same D , the rectification ratio is the largest for the SCn nanopore as seen in Figs. 4.6(B, C&D). The data shown in the plots also indicate a wider range of regimes accessible via variations in membrane biases for the cylindrical and SCn nanopores. This also corroborates our earlier assessment that single-conical nanopores with narrow openings in n -Si

E_g^{Si}	1.124 eV
$E_g^{SiO_2}$	9.0 eV
$q\chi_{Si}$	4.05 eV
$q\chi_{SiO_2}$	0.95 eV
ϵ_{Si}	11.70
ϵ_{SiO_2}	3.9
N_d^+	$2.0 \times 10^{20} \text{ cm}^{-3}$
N_a^-	$2.0 \times 10^{20} \text{ cm}^{-3}$
N_{surf}	$-4.0 \times 10^{20} \text{ cm}^{-3}$
T	300 K
ϵ_{KCl}	80.0
$[KCl]_0$	0.1 M

Table 4.1: Material parameters and constants. N_{surf} corresponds to the surface charge density $\sigma = -0.16 \text{ e/nm}^2$.

are better suited for control of a large molecule translocation.

Chapter 5

Poisson-Nernst-Planck approach

In this chapter, we demonstrate the proper discretization of the Nernst-Planck equations, with the description of the self-consistent iterative method.

After that, we apply the Poisson-Nernst-Planck method to several practical problems. We compare the complete 3D PNP method to the 1D model, which was used in the previous chapter. Then, the accuracy of the PNP method is checked with Ohm's law. The last part contains simulation results obtained for the cylindrical nanopore in a semiconductor membrane, which is made of three layers: SiO_2 – n-Si – SiO_2 . This nanopore is designed to resemble the traditional MOS field-effect transistors. The I-V characteristics and other properties of this ionic transistor are calculated and discussed.

5.1 Discretization of the Nernst-Planck equations.

5.1.1 Ionic current density.

The current density of the ionic species with valence Z and concentration distribution $c(\vec{r})$ in the electrolyte

$$\vec{J} = -q\mu c \nabla \varphi - qDZ \nabla c.$$

For Cl^- : $Z_{\text{Cl}} = -1$, $c = [\text{Cl}^-]$, and for K^+ : $Z_{\text{K}} = +1$, $c = [\text{K}^+]$.

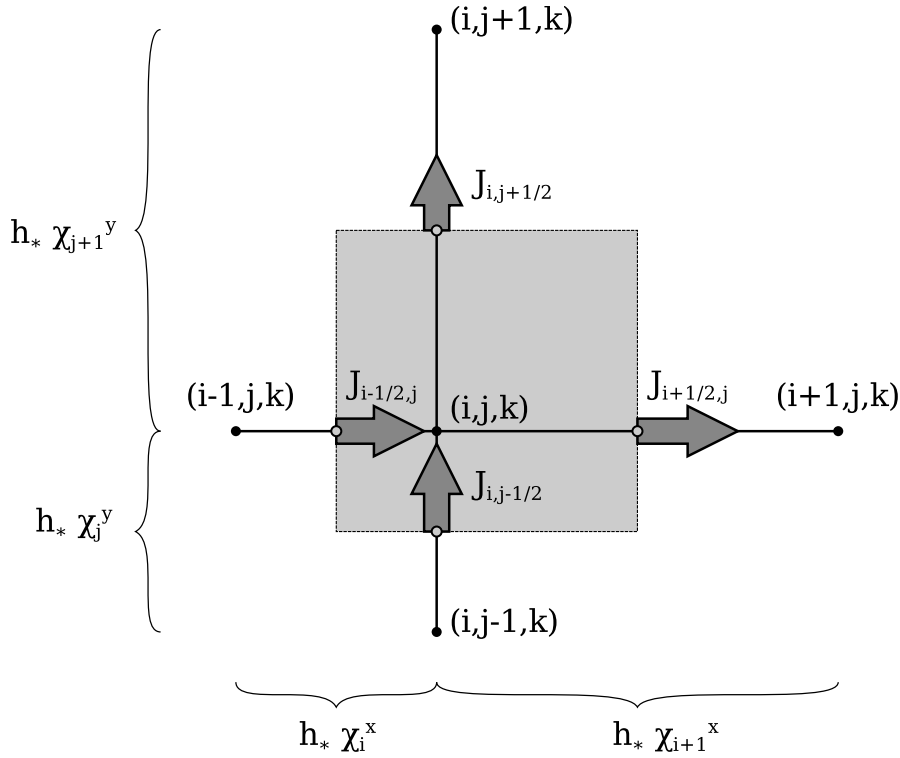


Figure 5.1: This picture is a small piece of the grid, centered on the grid-point (i, j, k) . Five small black circles represent the grid-point (i, j, k) itself, and its four neighbors: $(i+1, j, k)$, $(i-1, j, k)$, $(i, j+1, k)$, and $(i, j-1, k)$. Four big arrows are the current densities $J_{[i+1/2, j]}$, $J_{[i-1/2, j]}$, $J_{[i, j+1/2]}$, and $J_{[i, j-1/2]}$. They are defined at the "half-points", which are marked with the small white circles. The curly braces below and on the left side show distances between the grid-points. The shaded square is the "volume" of the grid-point (i, j, k) .

5.1.2 Finite-Difference Discretization.

Following [56], to solve Nernst-Planck equations, the current densities $J_{[i+1/2]}$ and $J_{[i-1/2]}$ should be used, they are defined in the following way:

$$\frac{J_{[i+1/2]}}{q} = (-\mu c \nabla \varphi - DZ \nabla c)|_{i+1/2} \approx -\mu \frac{c_{i+1} + c_i}{2} \cdot \frac{\varphi_{i+1} - \varphi_i}{h_i} - DZ \frac{c_{i+1} - c_i}{h_i}, \quad (5.1)$$

$$\frac{J_{[i-1/2]}}{q} = -\mu \frac{c_i + c_{i-1}}{2} \cdot \frac{\varphi_i - \varphi_{i-1}}{h_{i-1}} - DZ \frac{c_i - c_{i-1}}{h_{i-1}}, \quad (5.2)$$

where h_i is the distance between grid-point i and grid-point $i + 1$,

These current densities represent fluxes from i to $(i + 1)$ (equation 5.1), and from $(i - 1)$ to i (equation 5.2). Here, we have defined current densities only along the X axis (index i), however the same definitions should be applied to axes Y (index j) and Z (index k). In the Figure 5.1, four big arrows represent current densities $J_{[i+1/2, j]}$, $J_{[i-1/2, j]}$, $J_{[i, j+1/2]}$, and $J_{[i, j-1/2]}$.

Using the new notation, the steady state Nernst-Planck equations (in 1D) may be transformed into the finite-difference representation

$$\text{div} \vec{J} = 0 \quad \rightarrow \quad \frac{J_{[i+1/2]} - J_{[i-1/2]}}{(h_i + h_{i-1})/2} = 0. \quad (5.3)$$

5.1.3 Nernst-Planck equation in 1D.

If we introduce a common dimensional constant h_* for the grid (such as 0.1 nm, 1 nm, 1 μ m etc.), and multipliers χ_i specific to each layer of the grid, such that $h_i = h_* \chi_i$ (here, χ_i is equal to, for example, 1, 2, 4, 8, etc), the equation (5.3) can be rewritten:

$$\frac{J_{[i+1/2]} - J_{[i-1/2]}}{(h_* \chi_i + h_* \chi_{i-1})/2} = 0,$$

Taking into account (5.1) and (5.2):

$$\frac{1}{(h_*\chi_i + h_*\chi_{i-1})/2} \left(\left(-\mu \frac{c_{i+1} + c_i}{2} \cdot \frac{\varphi_{i+1} - \varphi_i}{h_*\chi_i} - DZ \frac{c_{i+1} - c_i}{h_*\chi_i} \right) - \left(-\mu \frac{c_i + c_{i-1}}{2} \cdot \frac{\varphi_i - \varphi_{i-1}}{h_*\chi_{i-1}} - DZ \frac{c_i - c_{i-1}}{h_*\chi_{i-1}} \right) \right) = 0$$

Therefore,

$$\begin{aligned} & c_i \cdot \frac{1}{h_*^2(\chi_i + \chi_{i-1})/2} \cdot \left(\frac{\mu}{2DZ} \left(\frac{\varphi_{i+1} - \varphi_i}{\chi_i} - \frac{\varphi_i - \varphi_{i-1}}{\chi_{i-1}} \right) - \left(\frac{1}{\chi_i} + \frac{1}{\chi_{i-1}} \right) \right) + \\ & c_{i+1} \cdot \frac{1}{h_*^2(\chi_i + \chi_{i-1})/2} \cdot \left(\frac{\mu}{2DZ} \frac{\varphi_{i+1} - \varphi_i}{\chi_i} + \frac{1}{\chi_i} \right) + \\ & c_{i-1} \cdot \frac{1}{h_*^2(\chi_i + \chi_{i-1})/2} \cdot \left(\frac{\mu}{2DZ} \frac{\varphi_i - \varphi_{i-1}}{\chi_{i-1}} + \frac{1}{\chi_{i-1}} \right) = 0 \end{aligned}$$

5.1.4 Nernst-Planck equation in 3D.

In 3D, Nernst-Planck equation is a sum of three 1D-equations for each direction x, y and z

$$\frac{J_{[i+1/2,j,k]} - J_{[i-1/2,j,k]}}{(h_*\chi_i^x + h_*\chi_{i-1}^x)/2} + \frac{J_{[i,j+1/2,k]} - J_{[i,j-1/2,k]}}{(h_*\chi_j^y + h_*\chi_{j-1}^y)/2} + \frac{J_{[i,j,k+1/2]} - J_{[i,j,k-1/2]}}{(h_*\chi_k^z + h_*\chi_{k-1}^z)/2} = 0$$

This is the linearization of the Nernst-Planck equations, unfortunately, we have obtained this equation only for grid points, which are located not on the boundaries. Therefore, it defines only a part of the matrix \mathbf{M}_c and the right-hand side vector (zero) for the system of linear equations $\mathbf{M}_c \mathbf{c} = \mathbf{rhs}_c$. Boundary conditions will be discussed in the following sections. The obtained system of linear equations, eventually, must be solved for concentrations c .

5.1.5 Nernst-Planck equation in 3D and Gauss's divergence theorem

Since $h_*\chi_i^x$ and $h_*\chi_{i-1}^x$ are distances between neighboring grid-points, the spatial dimensions of the grid-point (i,j,k) may be defined as follows

$$\Delta x_{i,j,k} = (h_*\chi_i^x + h_*\chi_{i-1}^x)/2$$

$$\Delta y_{i,j,k} = (h_*\chi_j^y + h_*\chi_{j-1}^y)/2$$

$$\Delta z_{i,j,k} = (h_*\chi_k^z + h_*\chi_{k-1}^z)/2$$

In Figure 5.1, $\Delta x_{i,j,k}$ and $\Delta y_{i,j,k}$ are, respectively, the width and the height of the shaded square. The volume of this grid point is $\Delta x_{i,j,k}\Delta y_{i,j,k}\Delta z_{i,j,k}$.

Nernst-Planck equation can be rewritten:

$$\frac{J_{[i+1/2,j,k]} - J_{[i-1/2,j,k]}}{\Delta x_{i,j,k}} + \frac{J_{[i,j+1/2,k]} - J_{[i,j-1/2,k]}}{\Delta y_{i,j,k}} + \frac{J_{[i,j,k+1/2]} - J_{[i,j,k-1/2]}}{\Delta z_{i,j,k}} = 0 \quad (5.4)$$

If the equation is multiplied by the grid-point volume $\Delta x_{i,j,k}\Delta y_{i,j,k}\Delta z_{i,j,k}$, we obtain the integral representation of the same equation (subscripts (i,j,k) are omitted):

$$\Delta y \Delta z (J_{[i+1/2,j,k]} - J_{[i-1/2,j,k]}) + \Delta x \Delta z (J_{[i,j+1/2,k]} - J_{[i,j-1/2,k]}) + \Delta x \Delta y (J_{[i,j,k+1/2]} - J_{[i,j,k-1/2]}) = 0 \quad (5.5)$$

This equation means that the total flux $\sum_{\kappa} (\vec{J}_{\kappa} \cdot \vec{Area}_{\kappa})$ through the grid-point's boundary must be equal to zero. The physical meaning of this equation is the conservation of ionic fluxes on the grid. Both equations (5.4) and (5.5) are equivalent, it means that Gauss's divergence theorem is applicable locally to each grid-point. Thus, total fluxes are conserved, moreover, the integral interpretation (5.5) of the Nernst-Planck equation provides a clear way to define boundary conditions.

5.1.6 Boundary Conditions

The finite-difference representation of the boundary conditions (section 3.2.4) are derived directly from the equations (5.5). If the point (i, j, k) is the electrolyte, and some of the six neighboring points belong to the solid-state membrane, the corresponding current densities in the equation (5.5) are set to be zero. For example, if $(i, j+1, k)$ grid point is not the electrolyte (e.g. SiO_2), then $J_{[i, j+1/2, k]} = 0$. Conservation of the total flux holds for any shape of the boundary. The same approach is used in publications [41–43].

The grid points on the boundary of the box are defined in the similar way. Since axis X corresponds to the axis of the membrane, points $x = -L_x/2$ and $x = L_x/2$ must have bulk concentrations, so simple Dirichlet conditions are $c(x = \pm L_x/2) = [KCl]_0$. Four other boundaries: $y = \pm L_y/2$ and $z = \pm L_z/2$, may be expressed using the same zero-flux conditions, as used for points of the electrolyte-membrane boundary, setting the current densities through the boundary equal to zero:

$$\begin{aligned} J_{[i, j+1/2, k]}|_{y=L_y/2} &= 0, & J_{[i, j-1/2, k]}|_{y=-L_y/2} &= 0, \\ J_{[i, j, k+1/2]}|_{z=L_z/2} &= 0, & J_{[i, j, k-1/2]}|_{z=-L_z/2} &= 0. \end{aligned}$$

5.1.7 Current through the pore in YZ cross-section.

The most apparent way to calculate the total ionic current through the pore, is to sum up fluxes through YZ cross-section at a half-point $i + 1/2$.

$$I(i + 1/2) = \sum_{j, k=0}^{j=N_j-1, k=N_k-1} \vec{J}_{[i+1/2, j, k]} \cdot \vec{A}_{[i+1/2, j, k]}$$

Area $\vec{A}_{[i+1/2,j,k]} = \hat{i}\Delta y\Delta z$.

And since $\vec{J} \cdot \hat{i}$ is equal to x component of the current density, J_x , the equation for total current inside the pore is the following

$$I(i+1/2) = \sum_{j,k} J_{x[i+1/2,j,k]} \cdot \frac{h_*^2 \cdot (\chi_j^y + \chi_{j-1}^y) \cdot (\chi_k^z + \chi_{k-1}^z)}{4} \quad (5.6)$$

5.2 Iterative method

5.2.1 Data representation

All data (such as φ , n , p , etc.) are stored in linear vectors $1 \times N_x N_y N_z$.

The norm for such data vectors is defined as a maximum absolute value of the vector's element

$$||v|| = \max |v_i|, \text{ where } i \text{ is the element's index.}$$

5.2.2 Convergence condition

The iterative process described below is repeated until:

- $||\varphi^t - \varphi^{t-1}|| < 10^{-7}$ V, and
- For all charge carriers concentrations $\frac{||\rho^t - \rho^{t-1}||}{||\rho^{t-1}||} < 10^{-7}$.

Here, the notation x^t and x^{t-1} stands for data x calculated at the iteration-step t and $t - 1$, respectively.

5.2.3 Iterative procedure

All the following actions are performed at *each* step of the iteration:

1. Define matrix **M** and right-hand-side vector **rhs** for Poisson's Equation. It is done by a simple linearization of the Poisson's Equation.

Optionally, Gummel's method is used by adding extra components to left- and right-sides of the equation:

$$\nabla(\varepsilon \nabla \varphi^t) + r^{t-1} \varphi^t = -\frac{\rho^{t-1}}{\varepsilon_0} + r^{t-1} \varphi^{t-1}, \text{ where}$$

$$\rho^{t-1} = q(-n + p - N_A^- + N_D^+ + N_{\text{surf}} - [Cl^-] + [K^+])$$

$$r^{t-1} = -\frac{q}{kT}[Cl^-] - \frac{q}{kT}[K^+] -$$

$$\frac{q}{kT} N_C^{eff} \mathcal{F}_{-1/2} \left(\frac{q(\varphi - \psi) - \frac{E_g}{2}}{kT} \right) - \frac{q}{kT} N_V^{eff} \mathcal{F}_{-1/2} \left(\frac{-q(\varphi - \psi) - \frac{E_g}{2}}{kT} \right)$$

2. Tolerance is determined for the iteration step:

$$\mathbf{tol}^t = 0.90 \cdot \mathbf{tol}^{t-1} + 0.10 \cdot (10^{-4} \cdot \|\varphi^{t-1} - \varphi^{t-2}\|)$$

The initial value for the first iteration is $\mathbf{tol}^0 = 10^{-5}$.

In addition, if obtained value is still rather big, i.e. $\mathbf{tol}^t > 10^{-3} \cdot \|\varphi^{t-1} - \varphi^{t-2}\|$,

$$\mathbf{tol}^t = 0.80 \cdot \mathbf{tol}^t + 0.20 \cdot (10^{-4} \cdot \|\varphi^{t-1} - \varphi^{t-2}\|)$$

Then, the value is constrained to be in the range $10^{-4} < \mathbf{tol}^t < 10^{-8}$.

3. The Poisson's equation

$$\mathbf{M} \tilde{\varphi}^t = \mathbf{rhs}$$

is solved using the Gauss-Seidel (G-S) or the Bi-conjugate gradient method (BiCG) with the tolerance \mathbf{tol}^t , and since both G-S and BiCG methods are iterative, no more than 1000 internal iterations is allowed for them.

4. The new φ^t is calculated as follows:

$$\varphi^t = \alpha \tilde{\varphi}^t + (1 - \alpha) \varphi^{t-1}, \text{ where}$$

the value $\tilde{\varphi}^t$ is obtained from the solution of the Poisson's equation.

The parameter α is not constant, but slowly increases with each iteration from 0.1 to 0.4:

$$\alpha = \min (0.1 \exp(0.06 \cdot t), \quad 0.4)$$

5. Then, the Nernst-Planck equations are solved for ionic concentrations, and concentration of electrons and holes are calculated from the Fermi-Dirac statistics. Alternatively, at this step, ionic concentrations may be calculated from Boltzmann's statistics, and thus, the purely electrostatic solution can be obtained:

- (a) The Nernst-Planck equations are transformed to the system of linear equations:

$$\mathbf{M}_c \tilde{\rho}^t = \mathbf{rhs}_c$$

They are solved using the Gauss-Seidel or Bi-Conjugate Gradient method with the tolerance 10^{-8} , a number of the internal method iterations is not larger than 500.

- (b) Concentrations of electrons and holes in semiconductor are calculated from the Fermi-Dirac statistics.

(c) New concentrations are:

$$c^t = \alpha_c \tilde{c}^t + (1 - \alpha_c) c^{t-1}, \text{ where } \alpha_c = 0.4.$$

5.3 One-dimensional method for ionic current calculation, and evaluation of its validity.

In the previous chapter (also see [49]), we demonstrated that ionic conductivity of the nanopore in a double-layered membrane may be efficiently controlled by the applied voltages V_n and V_p . The strongest current rectification with the diode-like I-V curves were obtained for $V_n = 0.8 \text{ V}$ and $V_p = -0.8 \text{ V}$, and almost linear I-V characteristics were achieved at $V_n = -0.8 \text{ V}$ and $V_p = 0.4 \text{ V}$. Although these results clearly demonstrate the capability of the semiconductor nanopore device, the technique used to evaluate currents was not very accurate: The Nernst-Planck equations were solved only in one dimension, in the assumption that non-zero voltage applied across the membrane ($V \equiv V_S - V_D$) modifies the electrostatic potential in the pore linearly: $\varphi(x) = \varphi_{ES}(x) + V_S + (V_D - V_S)x/L$ (L is the membrane thickness, and $0 \leq x \leq L$). Here, we check the validity of this approach, and compare I-V characteristics with solutions of the full three-dimensional Poisson-Nernst-Planck method.

The electrostatic potential φ_{ES} is obtained for a system in equilibrium, when equations of the electrostatic problem (3.1, 3.2, 3.3, 3.7, and 3.8) are solved self-consistently. The one-dimensional data $\varphi_{ES}(x)$ may be taken either from the center of the pore $\varphi_{ES}(x) = \varphi_{ES}(x, y, z)|_{y=0, z=0}$, or each point can be found as the average

potential $\langle \varphi_{ES}(x, y, z) \rangle$ over the corresponding YZ cross-section of the pore. The second method would, presumably, work better for wider nanopores with diameter larger than the doubled Debye length $D > 2\lambda_D$. In this section, we test both possibilities. The corresponding 1D methods of current estimation are referred to as “1D-center” and “1D-average” in figures and the text.

5.3.1 I-V characteristics of the 1D and 3D methods

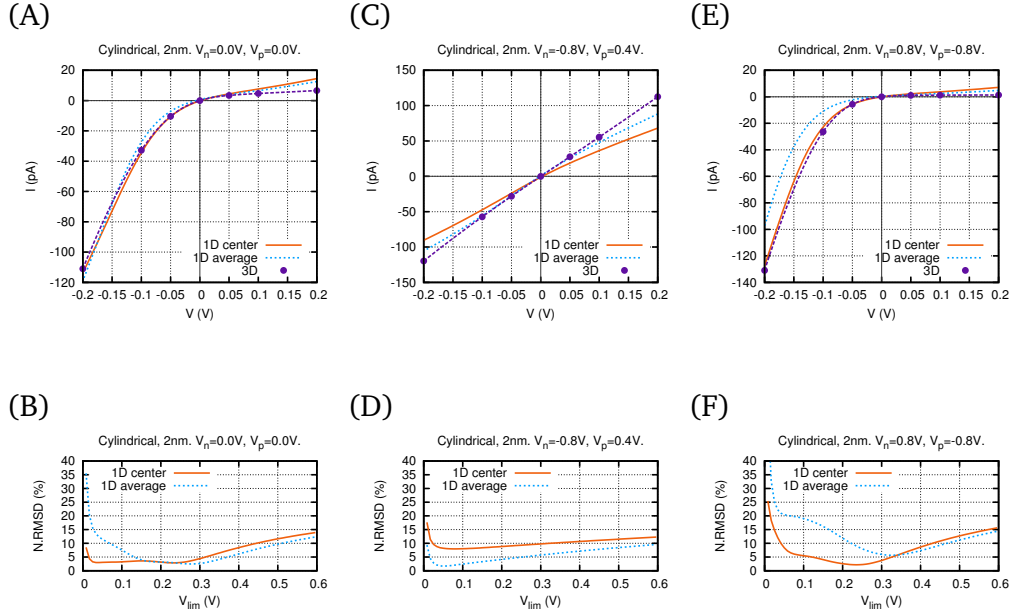


Figure 5.2: (A, C, E) I-V characteristics and (B, D, F) normalized deviations (5.8) of the 1D methods, calculated for the Cylindrical pore with the diameter $D = 2$ nm. Panels (A, B) correspond to zero voltages on the membrane; (C, D) V_n and V_p with ohmic, and (E, F) diode-like behavior.

I-V curves for a cylindrical geometry are shown in Figure 5.2 (plots corresponding to other geometries and voltages are shown in the Appendix A). In most cases both 1D methods produce quite good results, especially for small voltages $|V| < 0.1$ V applied across the membrane. However, for some voltages, estimated curves do not fit very well (such as in Figure 5.2 (E)). Simulations show that usually “1D-

center” method works better for negative V , which corresponds to forward bias in the diode-like I-V curves. The “1D-average” method is usually better for positive V (reverse bias), when current is saturated.

5.3.2 Quantitative estimation of the difference between 1D and 3D methods

To obtain a quantitative measure of the similarity between I-V curves, we calculate the root-mean squared deviation of the 1D solution $I(V)$ from the “ideal” $I_{3D}(V)$, or integral representation of this deviation:

$$\text{RMSD}[I(V)]_{(V_{lim})} = \sqrt{\frac{\sum_{|V| \leq V_{lim}} (I(V) - I_{3D}(V))^2}{\sum_{|V| \leq V_{lim}} 1}} \approx \sqrt{\frac{\int_{-V_{lim}}^{V_{lim}} (I(V) - I_{3D}(V))^2 dV}{2V_{lim}}} \quad (5.7)$$

Here, parameter V_{lim} defines a scope, in which the comparison is performed. We normalize $\text{RMSD}[I(V)]_{(V_{lim})}$ by the magnitude of $I_{3D}(V)$ variation in the region $|V| \leq V_{lim}$:

$$\text{N.RMSD}[I(V)]_{(V_{lim})} = \frac{\text{RMSD}[I(V)]_{(V_{lim})}}{\max_{|V| \leq V_{lim}} I_{3D}(V) - \min_{|V| \leq V_{lim}} I_{3D}(V)} \quad (5.8)$$

Here, continuous I-V characteristics of the 3D method $I_{3D}(V)$ were obtained via interpolation of the discrete data points with cubic splines (using the algorithm from the GNU Scientific Library).

Results are shown in the Table 5.1. For all geometries, we calculate the normalized RMS deviation for $V_{lim} = 0.1 \text{ V}$ and 0.2 V . Also, the complete plots of N.RMSD vs. V_{lim} are shown in the Appendix A.

The current in the cylindrical pore has errors less than 10% in most cases, except

Geometry	V_n	V_p	“Center”		“Average”	
			N.RMSD (%) estimated for V_{lim} :			
			0.1 V		0.1 V	
			0.2 V		0.2 V	
Cyl, 2 nm	0.0 V	0.0 V	3.3	3.1	7.5	3.2
	-0.8 V	0.4 V	8.0	8.8	2.4	4.2
	0.8 V	-0.8 V	5.5	2.5	19.0	11.8
DC, 6 nm	0.0 V	0.0 V	7.8	10.9	6.4	16.8
	-0.8 V	0.4 V	5.4	2.7	7.1	10.2
	0.8 V	-0.8 V	11.6	10.0	9.0	9.0
SCn, 6 nm	0.0 V	0.0 V	16.9	25.4	16.2	46.7
	-0.8 V	0.4 V	5.1	3.9	14.0	16.5
	0.8 V	-0.8 V	19.0	22.5	5.5	30.2
SCp, 6 nm	0.0 V	0.0 V	5.9	8.2	7.2	7.3
	-0.8 V	0.4 V	5.9	4.9	9.2	10.1
	0.8 V	-0.8 V	10.6	10.2	13.7	8.2

Table 5.1: Values of $N.RMSD[I(V)]_{(V_{lim})}$ for cylindrical, double-conical and two single-conical geometries, calculated for $V_{lim} = 0.1$ V and 0.2 V.

the most diode-like I-V ($V_n = 0.8 \text{ V}$, $V_p = -0.8 \text{ V}$). However, as it can be seen in Figure 5.2, the difference in this worst case is not extremely large, and the shape of the curve is the same. The DC and SCp geometries also demonstrate very good correspondence between 1D and 3D methods: The error rarely exceeds 10%.

5.4 Oxide Membrane.

To prove correctness of the simulations, we tested the program on a dielectric membrane with no surface charge. Such estimation is straight-forward if two facts are considered:

1. Cylindrical nanopore in such membrane must have uniformly distributed $[K^+] = [Cl^-] = [KCl]_0$, and the current is produced only by the drift component: $q\mu[KCl]_0\nabla\varphi$.
2. The magnitude of the electric field. The current of each ion species must be constant for each cross-section, and $I \propto \vec{E} \cdot A\vec{r}ea$. The size of the modeled system is approximately $17 \text{ nm} \times 17 \text{ nm} \times 53 \text{ nm}$, and the diameter of the pore is 2 nm , so the cross-sectional area is varying from 17^2 nm^2 outside to $\pi \text{ nm}^2$ inside the pore. The ratio of this areas is $17^2/\pi \approx 92$ ¹. Therefore, the electric field inside the pore is ≈ 92 times larger than outside the pore, and we safely can assume that the voltage drop is happening only inside the pore.

Using Ohm's law, the total current is

$$I(V) = 2q\mu[KCl]_0 \times (V/L) \times \pi R^2 \quad (5.9)$$

¹Moreover, ideally the area ratio must approach infinity, if a much larger volume is modeled.

Here, the factor of “2” is due to our assumption that both ion species have the same mobility μ , and their valences are $|Z| = 1$. The parameter L is the thickness of the membrane that is equal to 26 nm.

Comparison between simulation and 5.9 is shown in Figure 5.3. The estimation fits simulation results very well. Also, both used assumptions are correct: concentrations of ions indeed remain constant in the system, and electric potential is changing linearly in the pore, and is constant outside of it (not shown).

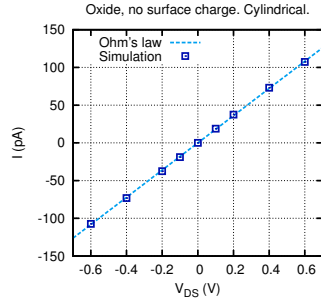


Figure 5.3: Current through the nanopore in a SiO_2 membrane that has no surface charge. The simulation result is in perfect agreement with the theory.

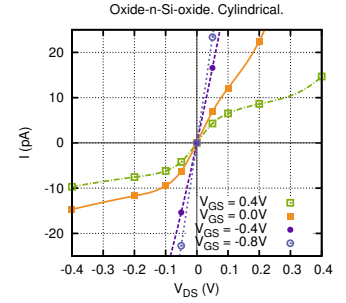
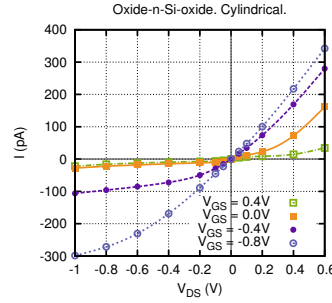


Figure 5.4: I-V curves for the Oxide-n-Si-oxide membrane: The full range of studied voltages on the left, and only small voltages ($|V_{DS}| < 0.4 \text{ V}$) on the right.

5.5 Oxide – n-Si – oxide Membrane.

Being inspired by Metal-Oxide-Semiconductor transistors devices, we propose the following design of the ionic transistor. The membrane is symmetric, and composed of three layers: SiO_2 , n-Si, and again SiO_2 as shown in Figure 5.5. The n-Si layers is 8 nm thick. The total membrane thickness is the same as before — 26 nm. We

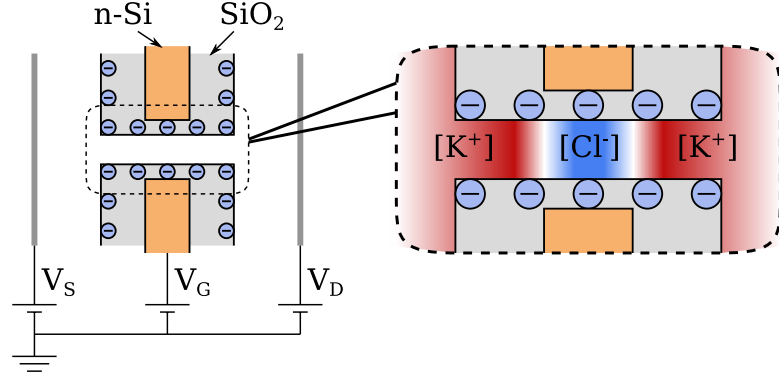


Figure 5.5: $\text{SiO}_2 - \text{n-Si} - \text{SiO}_2$ membrane, and the ionic distribution inside the channel for $V_G = 0$.

apply voltage V_G to the silicon layer, and it acts as a gate electrode on the electrolyte solution.

Two oxide layers play crucial part in this setup: The negative surface charge on the oxide-electrolyte boundary ($\sigma = -0.16e/nm^2$) attracts $[K^+]$ ions, making $[K^+] \approx 4 \times [KCl]_0$, and $[Cl^-] \approx 0.25 \times [KCl]_0$. Even larger separation is accessible, if the surface charge is larger, or if additional p-Si layers are added instead of SiO_2 , as it was done in [22], however, we try to keep the system not very complicated here.

The electrolyte inside the pore has three distinctive regions (Figure 5.5). Two regions within the oxide layers are similar to the heavily doped Source and Drain regions of the MOSFET, $[K^+] \gg [Cl^-]$. The central region is adjacent to n-Si, however is still insulated from it by a thin oxide layer. In unbiased state, $[Cl^-] > [K^+]$ in the central region, and the whole transistor is similar to an enhancement-mode p-channel MOSFET [53] (p. 362). A non-zero voltage V_G must be applied to turn it on.

Terminals that are applied to the electrolyte act as the Source and the Drain terminals. The geometry of our system has reflection symmetry with respect to the plane of the membrane, therefore, the difference between these two terminals is purely

nominal. We call the left terminal “Source”, V_S , and right is “Drain”, V_D . For all the following measurements, we assume that our ionic transistor and voltage sources form a common-source electric circuit.

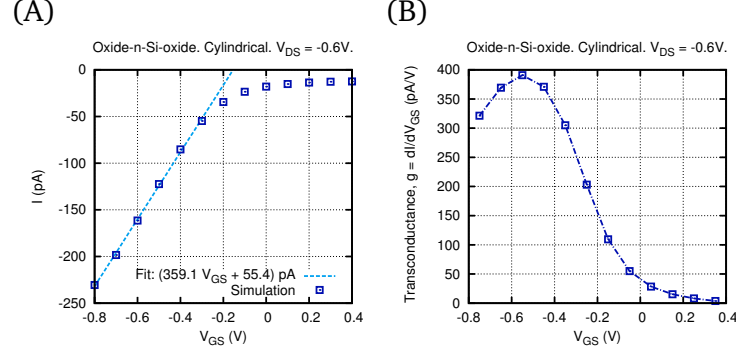


Figure 5.6: (A) Transfer characteristics. $I_{fit}(V_{GS}) = a \times V_{GS} + b$, where $a = 359 \pm 6 \text{ pA/V}$ and $b = 55 \pm 4 \text{ pA}$, (B) Transconductance $g = dI/dV_{GS}$ vs. V_{GS} . In both plots, the drain-source voltage $V_{DS} = -0.6 \text{ V}$.

5.5.1 I-V curves and transconductance.

I-V curves are shown in Figure 5.4. It can be seen clearly that for negative V_{DS} currents almost saturate (although, they still have a small slope). A negative gate voltage V_{GS} is necessary to increase this saturation current. The transfer characteristics is shown in Figure 5.6, it demonstrates the efficiency of the gate voltage: current starts increasing at $V_{GS} \approx -0.1 \text{ V}$ with almost constant transconductance $g \approx 359 \text{ pA/V}$. Unfortunately, current for $V_{GS} < 0.6 \text{ V}$ does not saturate at reasonable drain-source voltages, and it makes it difficult to estimate the exact shape of the transfer characteristics, it is possible that the ideal curve should be a quadratic function of V_{GS} [53] (p. 353), and not linear. However, in general, the device behavior is very similar to standard MOSFETs. The already saturated current slowly

increases with V_{DS} almost linearly (see Figure 5.4, and the output conductance in the Figure 5.7 (A)), which is similar to the channel-length modulation in MOSFETs, and the Early effect in Bipolar Junction Transistors (BJT).

More precise determination of characteristics may be done, probably, for nanopores with a larger surface charge, and larger layers thickness. Nevertheless, shown results are already very promising, and the original design can be enhanced to reveal other properties of the system, as well as to improve performance of the device.

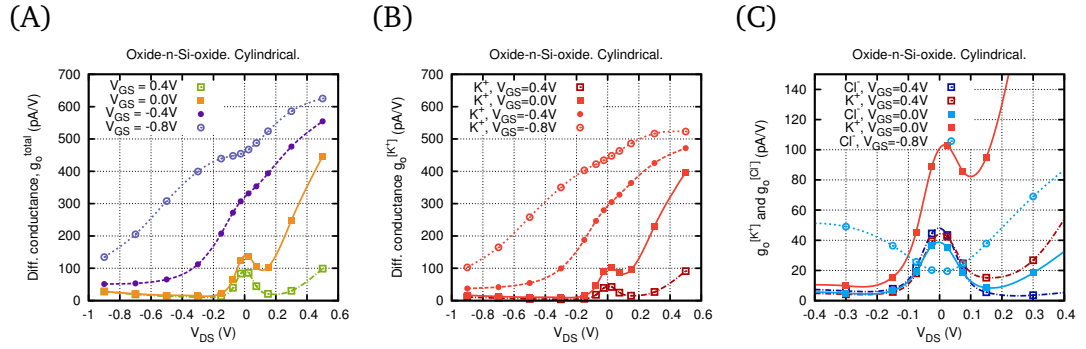


Figure 5.7: Output (differential) conductance $g_o = dI/dV_{DS}$ vs. V_{DS} . (A) g_o^{total} is calculated for the current of both ionic species, (B, C) $g_o^{[K^+]}$ and $g_o^{[Cl^-]}$ are calculated for $[K^+]$ and $[Cl^-]$ ionic currents separately.

5.5.2 Conductance for small drain-source bias V_{DS} .

Apart from the total ionic current flowing through the pore, it is reasonable to look at currents produced by each ionic species separately: $I^{[Cl^-]}$ and $I^{[K^+]}$. The total current $I = I^{[Cl^-]} + I^{[K^+]}$.

Then, we are able calculate the total Output (differential) conductance $g_o^{total} = dI/dV_{DS}$, and corresponding conductances for Cl^- and K^+ : $g_o^{[Cl^-]} = dI^{[Cl^-]}/dV_{DS}$, and $g_o^{[K^+]} = dI^{[K^+]}/dV_{DS}$. Plots of g_o vs. V_{DS} are demonstrated in Figure 5.7.

Now, we would like to investigate properties of the transistor for small V_{DS} . The case with positive gate voltage $V_{GS} = 0.4 \text{ V}$ is especially interesting: Although, on the larger scale, the I-V curve seems to be linear, in fact, it is not. It is shown in the right panel of the Figure 5.4 that there is a region of relatively high conductance for $|V_{DS}| < 0.1 \text{ V}$ (see also Figure 5.7 (A)).

The explanation can be found, if we look at the plots of concentration, which are shown in Figure 5.8. When magnitude V_{DS} is small, both $[Cl^-]$ and $[K^+]$ are non-zero, there is no depletion region inside the pore. However, when the applied drain-source bias is large enough (see second row in the Figure 5.8), concentrations are approaching zero, and the current becomes saturated. For $V_{GS} = 0.4 \text{ V}$ this is the case for both positive and negative V_{DS} . The system resembles two diodes connected as in a PNP BJT, and current quickly saturates for both directions of the drain-source voltage V_{DS} .

Also, we should note that $V_{GS} \leq -0.8 \text{ V}$ leads to almost opposite conductive properties: In the panel (C) of the Figure 5.7, conductance $g_o^{[Cl^-]}$ for $V_{GS} = -0.8 \text{ V}$ increases with larger $|V_{DS}|$. It happens, because the distribution of ions is completely different from the $V_{GS} = 0.4 \text{ V}$ case, and concentration of K^+ is high in the whole volume of the pore, and in addition, the Cl^- concentration in the channel increases with larger magnitudes of the drain-source voltage (see Figure 5.8).

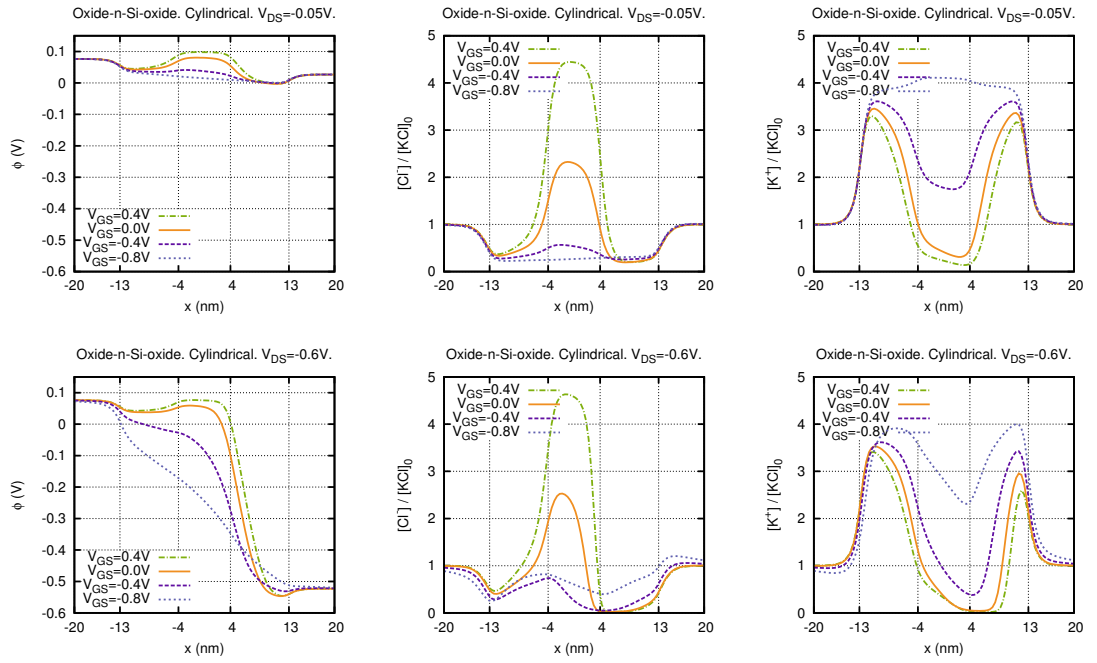


Figure 5.8: The electric potential and concentrations $[Cl^-]$ and $[K^+]$ at $V_{DS} = -0.05 \text{ V}$ (top row) and $V_{DS} = -0.6 \text{ V}$ (bottom row).

Conclusions

Electrostatic problem

In Chapter 4, we performed a general study of nanopores in a semiconductor membrane made of two layers of n-doped and p-doped Si material. In particular, we assessed our ability to change nanopore potential by applying voltage to the semiconductor membrane layers for different nanopore geometries: cylindrical, double conical and single conical. We considered only small pores with diameters of $2 - 10 \text{ nm}$, such that electric field induced by n-Si and p-Si layers significantly affects potential distribution in the pore, and consequently pore ionic conductivity. We demonstrate how variable voltages at the semiconductor layers V_n and V_p allow us to manipulate the potential, changing the pore potential landscape, which gives rise to ohmic (linear) or diode-like ionic current-voltage characteristics.

The data we obtained show a clear difference between current-voltage characteristics for pores with different diameters D . At the same time, the effect of the charge situated in the membrane as well as due to applied potential bias, doping, surface, etc. can also be significant. We find that the single-conical membrane with a narrow pore opening on the n-Si side allows for a wider range of potential variation in

the pore, and as such, can be better suited to exert control over a single molecule translocating through the pore. This is the case for our relatively small pores, diameter of which is comparable to the Debye length for physiological solution strengths ($1\text{ mM} - 1\text{ M}$).

Poisson-Nernst-Planck problem

In Chapter 5, the PNP approach was applied to simulate several devices with quite distinctive properties. Firstly, we tested the double-layered membrane from the Electrostatic problem, for which the 1D methods of current calculation were compared to the results of the 3D PNP method. The normalized RMS deviations (see Table 5.1) rarely exceed 10%, and only for SCn geometry they are larger than 20%.

After that, we checked the PNP method on the dielectric membrane, and then focused on the oxide – n-Si – oxide membrane, which was designed to resemble field-effect transistors from the traditional semiconductor electronics. We have shown that our ionic transistor has characteristics similar to MOSFETs, however more systematic investigation is necessary to determine details about the device behavior, and its capabilities to control ionic current. Different geometries and membrane structures must be tested. Our preliminary simulation results reveal that the double-conical geometry does not work very well for such a device, probably, because concentration of K^+ is not large enough in the channel. Nevertheless, research work in this direction may be productive, and new interesting results may be found.

Bibliography

- [1] Kasianowicz J J, Brandin E, Branton D and Deamer D W 1996 *Proc. Natl. Acad. Sci. USA*, **93**, 13770–3
- [2] Branton D et al 2008 *Nature Biotechnology* **26** 1146–53
- [3] Zwolak M and Di Ventra M 2008 *Rev. Mod. Phys.* **80** 141–65
- [4] Dekker C 2007 *Nature Nanotechnology* **2**, 209–15
- [5] Robertson J W F, Rodrigues C G, Stanford V M, Robinson K A, Krasilnikov O V and Kasianowicz J J 2007 *PNAS* **104** (20) 8207–11
- [6] Akeson M, Branton D, Kasianowicz J J, Brandin E and Deamer D W 1999 *Biophysical Journal* **77** 3227–33
- [7] Meller A, Nivon L, Brandin E, Golovchenko J and Branton D 2000 *Proc Natl Acad Sci USA* **97** (3) 1079–84
- [8] Wanunu M and Meller A 2007 *Nano Lett* **7**(6) 1580–5
- [9] Fologea D, Gershow M, Ledden B, McNabb D S, Golovchenko J A and Li J 2005 *Nano Lett* **5** (10) 1905–9
- [10] Lagerqvist J, Zwolak M and Di Ventra M 2007 *Biophysical Journal* **93** 2384–90

- [11] Striemer C C, Gaborski T R, McGrath J L and Fauchet P M 2007 *Nature* **445** 749–53
- [12] Han J, Fu J and Schoch R B 2008 *Lab Chip* **8** 23–33
- [13] Cruz-Chu E R, Aksimentiev A and Schulten K 2009 *J. Phys. Chem. C* **113** (5) 1850–62
- [14] He Y, Gillespie D, Boda D, Vlassiouk I, Eisenberg R S and Siwy Z S 2009 *J. Am. Chem. Soc.* **131** 5194–202
- [15] Karnik R, Castelino K and Majumdar A 2006 *Appl. Phys. Lett.* **88** 123114
- [16] Gracheva M E and Leburton J-P 2007 *Nanotechnology* **18** 145704
- [17] Vidal J, Gracheva M E and Leburton J-P 2007 *Nanoscale Res Lett* **2** 61–68
- [18] Kalman E B, Sudre O, Vlassiouk I and Siwy Z S 2009 *Anal Bioanal Chem* **394** 413–19
- [19] Nam S-W, Rooks M J, Kim K-B and Rossnagel S M 2009 *Nano Lett.* **9** (5) 2044–8
- [20] Siwy Z S and Howorka S 2010 *Chem. Soc. Rev.* **39** 1115–32
- [21] Gracheva M E, Vidal J and Leburton J-P 2007 *Nano Lett.* **7** (6) 1717–22
- [22] Gracheva M E, Melnikov D V and Leburton J P 2008 *ACS Nano* **2** (11) 2349–55
- [23] Zwolak M and Di Ventra M 2005 *Nano Lett* **5** 421–424
- [24] Lagerqvist J, Zwolak M and Di Ventra M 2006 *Nano Lett* **6** 779–782.

- [25] Jiang Z, Mihovilovic M, Chan J and Stein D 2010 *J Phys: Condens Matter* **22** 454114
- [26] Minot E D, Janssens A M, Heller I, Heering H A, Dekker C, and Lemay S G 2007 *Appl. Phys. Lett.* **91** 093507
- [27] Liu Y and Dutton R W 2009 *J. Appl. Phys.* **106** 014701
- [28] Landheer D, Aers G, McKinnon W R, Deen M J, and Ranuarez J C 2005 *Journal of Applied Physics* **98** 044701
- [29] Heitzinger C, Kennell R, Klimeck G, Mauser N, McLennan M, and Ringhofer C 2008 *J. Phys.: Conf. Ser.* **107** 012004
- [30] Bergveld P 2003 “ISFET, Theory and Practice” *IEEE Sensor Conference Toronto, October 2003*
- [31] Bergveld P 2003 *Sensors and Actuators B: Chemical* **88** (1) 1–20
- [32] Kal S, Bhanu P V 2007 “Design and modeling of ISFET for pH sensing” *TEN-CON 2007 - 2007 IEEE Region 10 Conference*
- [33] Schoch R, Han J, and Renaud P 2008 *Reviews of Modern Physics* **80** (3) 839–83
- [34] Larson I and Attard P 2000 *Journal of Colloid and Interface Science* **227** 152–63
- [35] Gentil C, Cote D, Bockelmann U 2006 *phys. stat. sol. (a)* **203** (14) 3412–6
- [36] Kirby Brian J *Micro- and Nanoscale Fluid Mechanics: Transport in Microfluidic Devices*
- [37] Rice C L and Whitehead R 1965 *J Phys Chem* **69** (11) 4017–24

- [38] Yao S, Santiago J G 2003 *Journal of Colloid and Interface Science* **268** (1) 133–42
- [39] Liu Y, Sauer J, and Dutton R W 2008 *Journal Of Applied Physics* **103** 084701
- [40] Cheng L-J and Guo L J 2007 *Nano Lett* **7** (10) 3165–71
- [41] Corry B, Kuyucak S, and Chung S H 2000 *Biophys J* **78** (5) 2364–81.
- [42] Kurnikova M G, Coalson R D, Graf P, and Nitzan A 1999 *Biophys J* **76** 642–56
- [43] Cardenas A E, Coalson R D, and Kurnikova M G 2000 *Biophys J* **79** 80–93
- [44] Coalson R D and Kurnikova M G 2005 *IEEE Trans Nanobioscience* **4** (1) 81–93
- [45] Gardner C L, Jerome J W, and Eisenberg R S 2002 *J Theor Biol* **219** 291–9
- [46] Gardner C L, Nonner W, and Eisenberg R S 2004 *Journal of Computational Electronics* **3** 25–31
- [47] Pandey S, Bortei-Doku A, and White M H 2007 *Comput Methods Programs Biomed* **85** (1) 1–7
- [48] Millar C, Roy S, Beckstein O, Sansom M S P, and Asenov A 2007 *J Comput Electron* **6** 367–71
- [49] Nikolaev A and Gracheva M E 2011 *Nanotechnology* **22** 165202
- [50] Gracheva M E, Xiong A, Aksimentiev A, Schulten K, Timp G and Leburton J-P 2006 *Nanotechnology* **17** 622
- [51] Ramírez P, Mafé S, Aguilera V M, Alcaraz A 2003 *Phys. Rev. E* **68** 011910(1)-011910(8)

- [52] Ramirez P, Apel P Yu, Cervera J and Mafe S 2008 *Nanotechnology* **19** 315707
- [53] Casey H C Jr 1999 *Devices for Integrated Circuits: silicon and III-V compound semiconductors* (New York: John Wiley & Sons) p 38–40
- [54] Kim R and Lundstrom M 2008 *Notes on Fermi-Dirac Integrals (3rd Edition)*
<http://nanohub.org/resources/5475>
- [55] Liu Y, Huber D and Dutton R 2010 *Appl. Phys. Lett.* **96** 253108
- [56] Selberherr S 1984 *Analysis and Simulation of Semiconductor Devices* (Springer-Verlag/Wien)
- [57] Lundstrom M S, Datta S, Schuelke R J, Bandyopahyey S, Sorlie P H 1984 *Physics and Modeling of Heterostructure Semiconductor Devices* Technical Report TR-EE 84-35 (School of Electrical Engineering, Purdue University, West Lafayette, IN)
- [58] Press W H, Teukolsky S A, Vetterling W T, Flannery B P 2007 *Numerical Recipes. The Art of Scientific Computing. 3rd Edition* (Cambridge University Press; 3 edition)

Appendix A

Comparison of I-V curves obtained from 1D and 3D methods, and the quantitative estimation of their difference.

This plots correspond to the data shown in the Table 5.1.

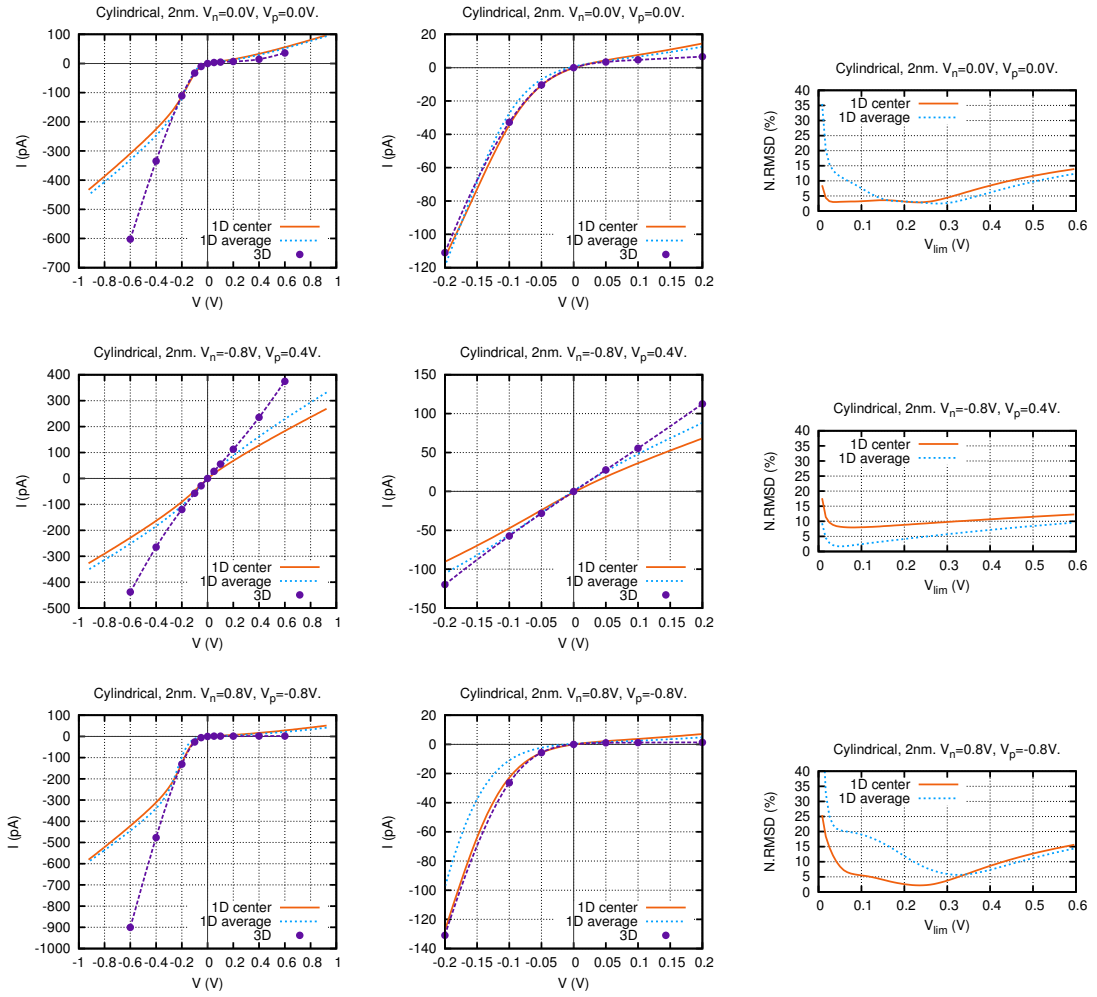


Figure A.1: *Cylindrical geometry.*

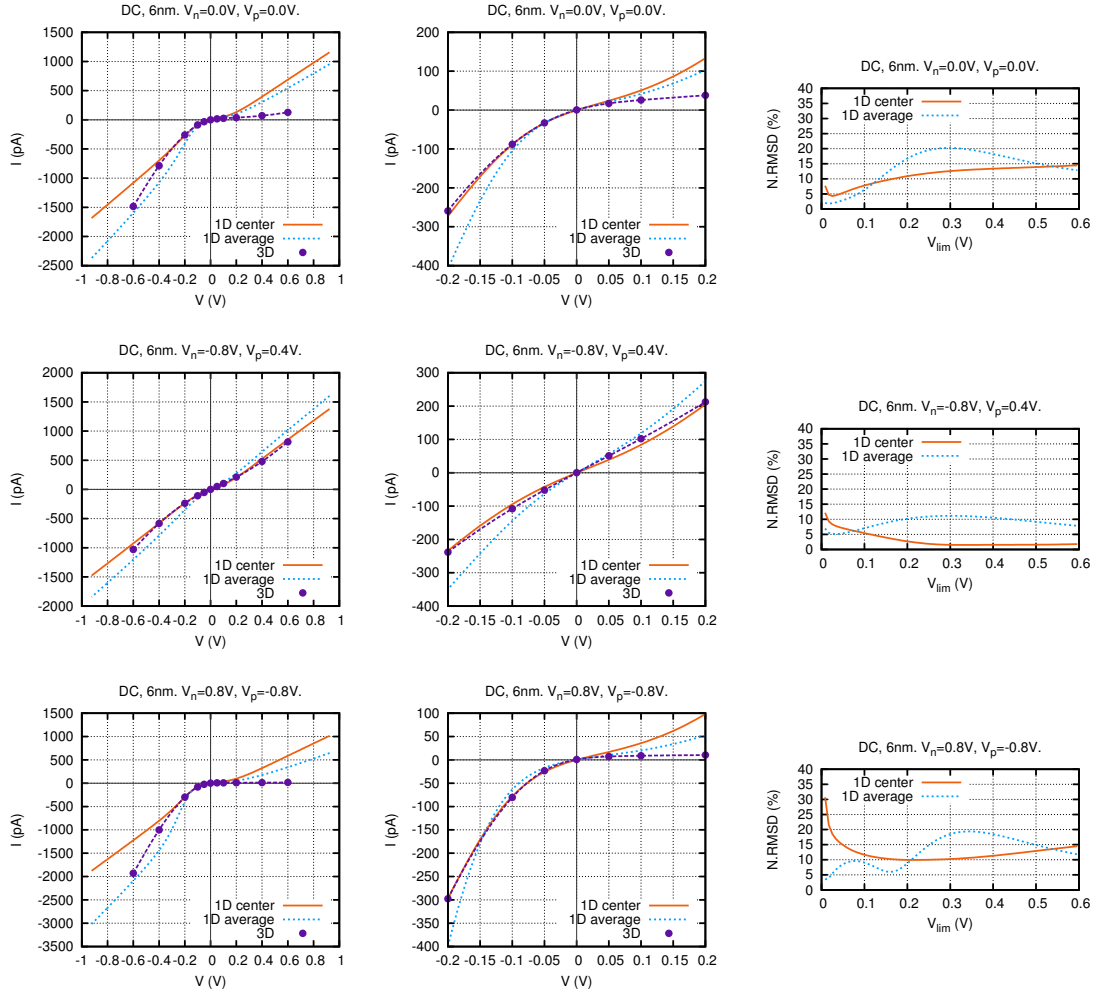


Figure A.2: Double-conical geometry, $D = 6$ nm.

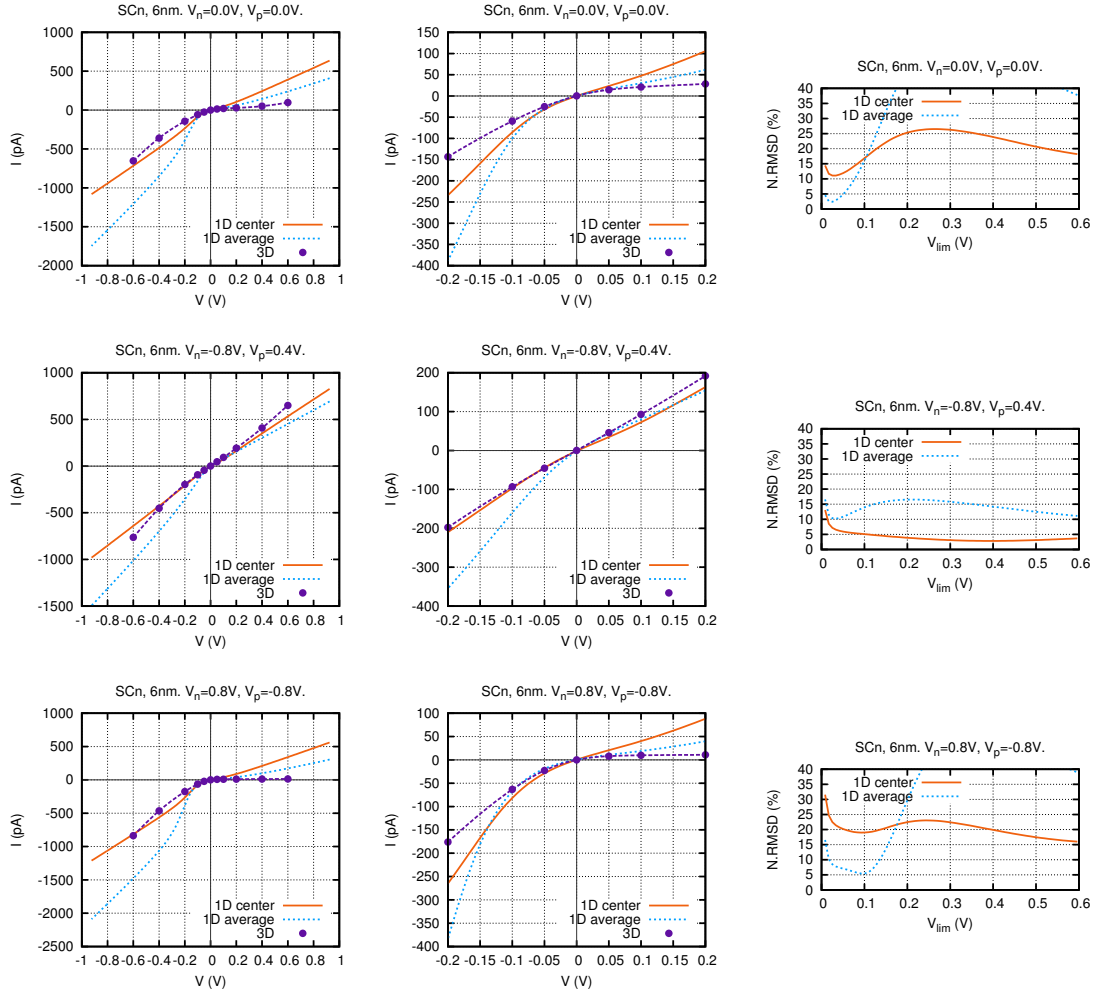


Figure A.3: Single-conical (SCn) geometry, $D = 6$ nm.

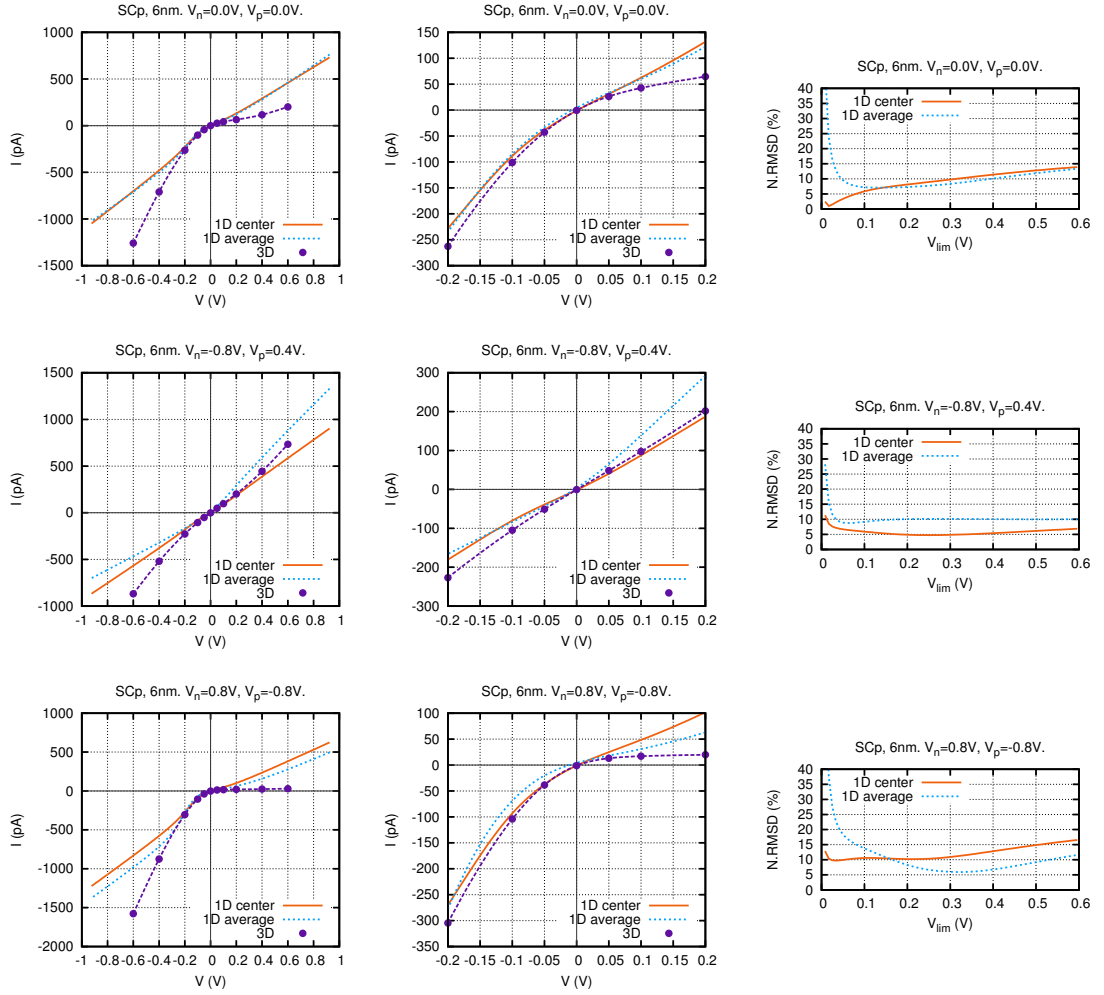


Figure A.4: Single-conical (SCp) geometry, $D = 6$ nm.